

### Nuclear Reaction Screening, Weak Interactions, and r-process Nucleosynthesis in High Magnetic Fields

Michael Famiano <sup>1,2</sup>, A. Baha Balantekin<sup>2,3</sup>, T. Kajino<sup>2,4,5</sup>, M. Kusakabe<sup>5</sup>, K. Mori<sup>2,4</sup>, and Y. Luo<sup>2,4</sup>, National Astronomical Observatory of Japan, Mitaka, Tokyo 181-8588, Japan, kajino@nao.ac.jp, kanji.mori@grad.nao.ac.jp, ydong.luo@grad.nao.ac.jp Department of Physics, University of Wisconsin, Madison, WI 53706, USA; baha@physics.wisc.edu

<sup>4</sup> Graduate School of Science, The University of Tokyo, 7-3-1 Hongo, Bunkyo-ku, Tokyo 113-0033, Japan

<sup>5</sup> School of Physics, and International Research Center for Big-Bang Cosmology and Element Genesis, Beihang University, 37 Xueyuan Rd., Haidian-district, Beijing 100083, People's Republic of China; kusakabe@buaa.edu.cn

\*\*Received 2020 June 14; accepted 2020 June 24; published 2020 August 4\*\*

#### Abstract

Coulomb screening and weak interactions in a hot, magnetized plasma are investigated. Coulomb screening is evaluated in a relativistic thermal plasma in which electrons and positrons are in equilibrium. In addition to temperature effects, effects on weak screening from a strong external magnetic field are evaluated. In high fields, the electron transverse momentum components are quantized into Landau levels. The characteristic plasma screening length at high temperatures and at high magnetic fields is explored. In addition to changes to the screening length, changes in weak interaction rates are estimated. It is found that high fields can result in increased  $\beta$ -decay rates as the electron and positron spectra are dominated by Landau levels. Finally, the effects studied here are evaluated in a simple r-process model. It is found that relativistic Coulomb screening has a small effect on the final abundance distribution. While changes in weak interaction rates in strong magnetic fields can have an effect on the r-process evolution and abundance distribution, the field strength required to have a significant effect may be larger than what is currently thought to be typical of the r-process environment in collapsar jets or neutron star mergers. If r-process sites exist in fields  $\gtrsim 10^{14}$  G, effects from fields on weak decays could be significant.

Unified Astronomy Thesaurus concepts: R-process (1324); Nucleosynthesis (1131); Magnetars (992); Magnetic fields (994); Magnetic stars (995)

### 1. Introduction

Nearly all modern nuclear astrophysics studies rely on knowledge of thermonuclear reaction rates (TRRs) between two or more reacting particles. The rate at which nuclei in a hot plasma interact is governed by the reaction cross section and the velocities of the reacting nuclei in their center of mass. In general, the reaction rates for an environment at a certain temperature are taken as the average rates, which are deduced by integrating over the reaction cross section (as a function of energy) weighted by the Maxwell–Boltzmann energy distribution of the reactants in the plasma involved, known as the TRR,  $\langle \sigma v \rangle$  (Illiadis 2007; Boyd 2008). For resonances in the cross section at specific energies, the evaluation is similar, but the cross section also has a term defining the resonance.

In a hot plasma, the background electrons create a "screening" effect between two reacting charged particles (Salpeter 1954; Salpeter & van Horn 1969; Dewitt et al. 1973; Graboske et al. 1973; Itoh et al. 1977; Jancovici 1977; Wallace et al. 1982; Shalybkov & Yakovlev 1987; Adelberger et al. 1998; Shaviv & Shaviv 2000; Quarati & Scarfone 2007; Wang et al. 2011; Potekhin & Chabrier 2013; Kravchuk & Yakovlev 2014; Liu 2016; Spitaleri et al. 2016; Wu & Pálffy 2017). Coulomb screening reduces their Coulomb barrier because the effective charge between two particles is reduced. The commonly used "extended" (Itoh et al. 1977; Jancovici 1977) screening and recent evaluations of screening from relativistic effects have been explored (Famiano et al. 2016; Luo et al. 2020). In evaluating the screening effect, even a small shift in the potential energy can result in significant changes in the classical turning points of the WKB approximation, resulting in an increase in the reaction rate. It should be noted that other positively charged nuclei in a plasma also increase the reaction rate as positive and negative charges are

redistributed in the presence of a "point-like" nuclear potential. Though this adjustment to thermonuclear rates has been known for a long time (Salpeter 1954), effects from relativistic, magnetized plasmas have not been fully addressed.

Closely tied to the equilibrium abundances of electrons and positrons is pair production, which occurs at high-enough temperatures in which the tail of the Fermi distribution exceeds the pair-production threshold. Pair production has been studied in stellar cores of very massive stars (Kozyreva et al. 2017; Spera & Mapelli 2017; Woosley 2017; Takahashi et al. 2018) and as a neutrino cooling mechanism (Itoh et al. 1996). Also, though electron capture reactions have been previously studied (Itoh et al. 2002; Liu et al. 2007), the simultaneous effects of external magnetic fields and relativistic pair production on reaction rate screening (fusion and electron capture) in magnetized plasmas have not been fully considered. For temperatures and magnetic fields that are high enough, electrons and positrons can exist in non-negligible equilibrium abundances. In a magnetized plasma, the electron and positron energy distributions are altered by the external field.

In a hot plasma, the background charges include the surrounding electrons, positrons, and other nuclei. Classically, for a nonrelativistic charge-neutral medium, the electrostatic potential  $\phi$  of a charge Ze in the presence of a background charge density can be computed via the Poisson–Boltzmann equation:

$$\nabla^2 \phi(r) = -4\pi Z e \delta(\mathbf{r}^3) - 4\pi \sum_{z \ge -1} z e n_z \exp\left[-\frac{z e \phi(r)}{T}\right], \quad (1)$$

where the last term is a sum over all charges in the medium with charge ze and number density  $n_z$ , including nonrelativistic electrons (z = -1). This description is almost universally used in astrophysical calculations involving nuclear reactions. Here,

the electron degeneracy must be calculated or estimated explicitly to accurately determine the energy and density distribution. (Natural units are used:  $k = \hbar = c = 1$ .)

However, for hot, magnetized plasmas, electrons and positrons must be expressed in equilibrium using Fermi–Dirac statistics. The lepton number density in the presence of an external field is modified by the presence of Landau levels and changes from the zero-field form (Grasso & Rubinstein 2001; Kawasaki & Kusakabe 2012):

$$n(B = 0, T) = \frac{1}{\pi^2} \int_0^\infty \frac{p^2 dp}{\exp\left[\frac{E - \mu}{T}\right] + 1} - \frac{1}{\pi^2} \int_0^\infty \frac{p^2 dp}{\exp\left[\frac{E + \mu}{T}\right] + 1},$$

$$n(B \neq 0, T) = \frac{eB}{2\pi^2} \sum_{n=0}^\infty (2 - \delta_{n0})$$

$$\times \left[ \int_0^\infty \frac{dp_z}{\exp\left[\frac{\sqrt{E^2 + 2neB} - \mu}{T}\right] + 1} - \int_0^\infty \frac{dp_z}{\exp\left[\frac{\sqrt{E^2 + 2neB} + \mu}{T}\right] + 1} \right]. \tag{2}$$

In the above Equation,  $E=\sqrt{p_z^2+m^2}$ , where the z-direction is parallel to the magnetic field. The term  $\delta_{n0}$  accommodates the degeneracy for the higher Landau levels, and the index n takes into account the Landau level as well as the z-component of electron spin. As  $B\to 0$ , the summation in the second relationship in Equation (2) becomes an integral, and the zero-field number density results.

The Poisson–Boltzmann equation must then be replaced with the equivalent equation assuming Fermi statistics with a magnetic field, B, and chemical potential,  $\mu$ :

$$\nabla^{2}\phi(r) = -4\pi Ze\delta^{3}(\mathbf{r}) - 4\pi \sum_{z>0} zen_{z} \exp\left[-\frac{ze\phi_{r}}{T}\right]$$

$$+ \frac{eB}{\pi} \sum_{n=0}^{\infty} g_{n} \int_{0}^{\infty} dp \left[\frac{1}{\exp\left[\frac{\sqrt{E^{2} + 2neB} - \mu - e\phi_{r}}{T}\right] + 1}\right]$$

$$- \frac{1}{\exp\left[\frac{\sqrt{E^{2} + 2neB} + \mu + e\phi_{r}}{T}\right] + 1}\right] + 4\pi \sum_{z>0} zen_{z}$$

$$- \frac{eB}{\pi} \sum_{n=0}^{\infty} g_{n} \int_{0}^{\infty} dp \left[\frac{1}{\exp\left[\frac{\sqrt{E^{2} + 2neB} - \mu}{T}\right] + 1}\right]$$

$$- \frac{1}{\exp\left[\frac{\sqrt{E^{2} + 2neB} + \mu}{T}\right] + 1}$$

$$(3)$$

where the sum in the third term accounts for the quantized transverse momentum of electrons and positrons in a high magnetic field, and  $g_n=2-\delta_{n0}$  accounts for Landau level degeneracy. The relativistic effects come from the high thermal energy,  $T\sim m_e$ , the Landau level spacing for field strengths with  $\sqrt{eB}\sim m_e$ , or both (Grasso & Rubinstein 2001; Kawasaki & Kusakabe 2012). The last two terms in Equation (3) account for the redistribution of charge on the uniform charge background. For a charge-neutral plasma, the sum of these last two terms is zero before the charge Ze is introduced. Here, electrons are assumed to be relativistic, while ions are still treated classically; the nonrelativistic nuclei are treated with Boltzmann statistics.

At lower temperatures and higher densities, the electron degeneracy is higher, and a first-order solution to the Poisson equation is invalid. The chemical potential must be accounted for in the relativistic treatment of Equation (3) and computed using the electron–positron number density assuming charge neutrality. The screening is very strong, and  $E_C/kT \gg 1$ . The thermal energy is less important, and the potential is modified by the difference in Coulomb energy before and after the reaction—the so-called ion-sphere model (Salpeter 1954; Salpeter & van Horn 1969; Clayton 1983).

Perhaps "intermediate screening," where  $E_C/kT \sim 1$ , is the most complicated. In this regime, screening enhancement has been computed in one of two ways. One method is to solve the Poisson–Boltzmann equation numerically (Graboske et al. 1973). In this case, numerical fits or tables might be used for astrophysical codes. For many computational applications, an empirical interpolation between strong and weak screening is computed (Salpeter & van Horn 1969; Wallace et al. 1982).

The "screening enhancement factor" f, relates the screened rate to the unscreened rate by  $\langle \sigma v \rangle_{\rm scr} = f \langle \sigma v \rangle_{\rm uns}$ . The value of f can be deduced from the WKB approximation in the TRRs as  $f = e^H$  (Salpeter 1954; Salpeter & van Horn 1969; Graboske et al. 1973; Jancovici 1977; Wallace et al. 1982), where H is a unitless value derived from the specific type of screening employed (Dewitt et al. 1973; Itoh et al. 1977; Alastuey & Jancovici 1978; Quarati & Scarfone 2007; Kravchuk & Yakovlev 2014; Sahoo & Das 2016). As mentioned above, the intermediate exponent  $H_I$  is often determined using strong and weak screening values,  $H_I = H_S H_W / \sqrt{H_S^2 + H_W^2}$ . This method is used commonly in astrophysics codes incorporating nuclear reaction networks (Meyer & Adams 2007; Paxton et al. 2011, 2015, 2018).

An example of the importance of including thermal and magnetic field effects is shown in Figure 1. Shown in the figure is the ratio of positron to electron number density as a function of temperature and magnetic field (where  $T_9$  is the temperature in billions of kelvin) at a density and electron fraction  $\rho Y_e = 5 \times 10^5 \text{ g cm}^{-3}$  taking into account the electron chemical potential at high density. Relativistic effects become increasingly important in this region as the positron number density becomes a significant fraction of the electron number density. The increased overall number of charges of any sign contribute to the screening effect, and this will be explored in this paper.

The goal of this paper is to evaluate the effects of reaction rate screening in relativistic electron-positron plasmas found in hot, magnetized stellar environments. Results from this work will be applied to an example nucleosynthesis process in a

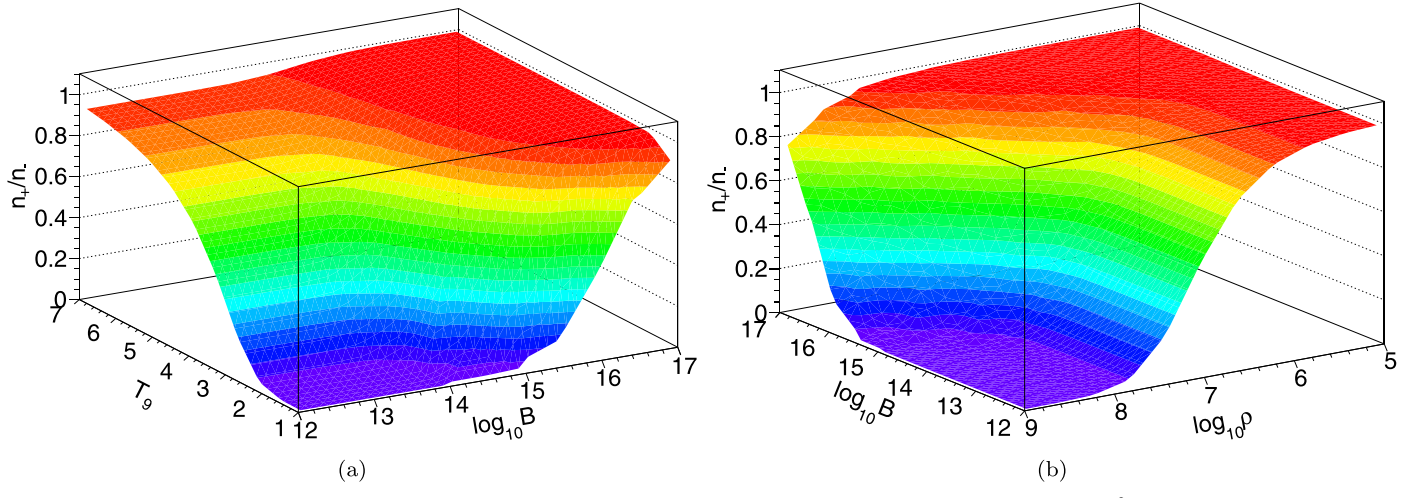


Figure 1. (a) Positron–electron ratio as a function of temperature and magnetic field in a neutral plasma at  $\rho Y_e = 5 \times 10^5$  g cm<sup>-3</sup>. (b) Positron–electron ratio as a function of density and magnetic field in a neutral plasma at temperature  $T_9 = 7$  and  $Y_e = 0.5$ . The number densities are computed up to 2000 Landau levels.

magnetohydrodynamic (MHD) collapsar jet. In this paper, the effects of weak screening corrections in a magnetized, relativistic plasma will be evaluated. A useful approximation that can be used effectively in computational applications is developed. The effects of screening in a sample astrophysical site are evaluated. In addition, the effects of strong magnetic fields on the weak interactions in a plasma are explored.

### 2. Weak Screening Limit

### 2.1. First-order Expansions: Debye–Hückel and Thomas– Fermi

In the high-temperature, low-density "weak screening" limit, the Coulomb energy between two reacting nuclei is lower than the thermal energy,  $E_C/kT \ll 1$ , as is the electron chemical potential. The electrons are mostly nondegenerate, and Equations (1) and (3) can be expanded to first order in potential,  $\mathcal{O}(\phi)$ , known as the Debye–Hückel approximation. A corresponding Debye length,  $\lambda_D$  can be derived, resulting in a Yukawa-type potential,  $\phi(r) \propto (e^{-r/\lambda_D})/r$  as opposed to the usual 1/r unscreened Coulomb relationship. For lower temperatures and higher densities resulting in higher electron degeneracy, the Thomas–Fermi (TF) screening length is more appropriate. This is defined by the first-order approximation:

$$\frac{1}{\lambda_{\rm TF}^2} \equiv 4\pi e^2 \frac{\partial n}{\partial \mu}.\tag{4}$$

This is derived from the density of states at the Fermi surface (Ichimaru 1993), but it is also equivalent to the first-order expansion in potential as the chemical potential is used as a mathematical surrogate for the potential with the same results. This relationship can also be deduced from the solution of the Schwinger–Dyson equation for the photon propagator (Kapusta & Gale 2006). The contribution to the screening length from the surrounding nuclei must also be included, and this can be significant in some cases.

The chemical potential can be determined using Equation (2) for a plasma of density  $\rho$ , electron fraction  $Y_e$ , and net electron

density  $n_- - n_+$ . For most astrophysical applications, a static plasma is assumed with a net charge density of zero.

The ratio of the relativistic Thomas–Fermi electron–positron screening length,  $\lambda_{\rm TF}$ , to the classical Debye length,  $\lambda_D$ , is shown in Figure 2 as a function of temperature and magnetic field at  $\rho Y_e = 5 \times 10^6$  g cm<sup>-3</sup>. In this figure, only the electron–positron screening length ratio is shown to emphasize the difference that high temperature and magnetic fields can induce in a plasma. In astrophysical calculations, the screening length from other nuclei must also be included,  $1/\lambda^2 = 1/\lambda_{\rm ion}^2 + 1/\lambda_{\rm ion}^2$ . There is a significant difference between the classical and relativistic screening lengths at high temperature and field. Because the screened rates depend exponentially on the screening lengths at low density/high temperature, even small changes in the screening length can be significant. The relativistic electron screening length can be quite small at highenough temperatures or B field.

It is noted that at higher density or lower temperature, intermediate screening depends more heavily on the electron chemical potential. The increased electron chemical potential results in the electron–positron number densities, which approach classical (nonrelativistic) values. That is  $n_- \to \rho N_A Y_e$  and  $n_+ \to 0$ . Because of this, first-order weak screening is replaced by an ion-sphere screening model or a type of geometric mean between the ion-sphere and weak screening models (Salpeter & van Horn 1969; Wallace et al. 1982).

In determining the equilibrium electron–positron number density and the screening lengths, computational models may truncate the number of Landau levels that are counted in the evaluation, or the sum may be replaced by an integral in a low-field approximation (Kawasaki & Kusakabe 2012). For high fields, one can determine the number of Landau levels necessary to sum over to obtain a certain accuracy in the computation. This is illustrated in Figure 3. In Figure 3(a), the computed electron chemical potential is shown as a function of the maximum Landau level,  $N_{\rm max}$  included in the sum in Equation (2) for  $T_9=2$ , and  $\rho Y_e=5\times 10^4~{\rm g\,cm}^{-3}$ . As the number of Landau levels summed over increases, the chemical potential converges to its equilibrium value. For a field of

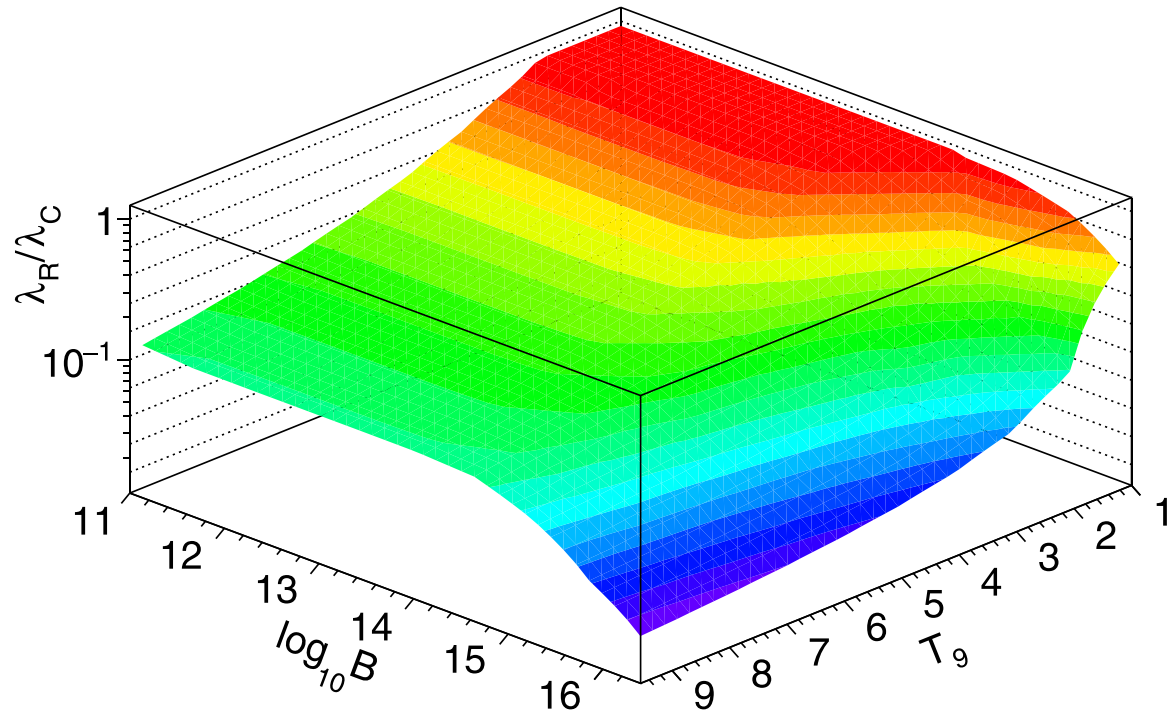


Figure 2. The ratio of classical to relativistic electron screening lengths for a neutral plasma as a function of temperature and magnetic field (G) at a constant electron density,  $\rho Y_e = 5 \times 10^5 \text{ g cm}^{-3}$ .

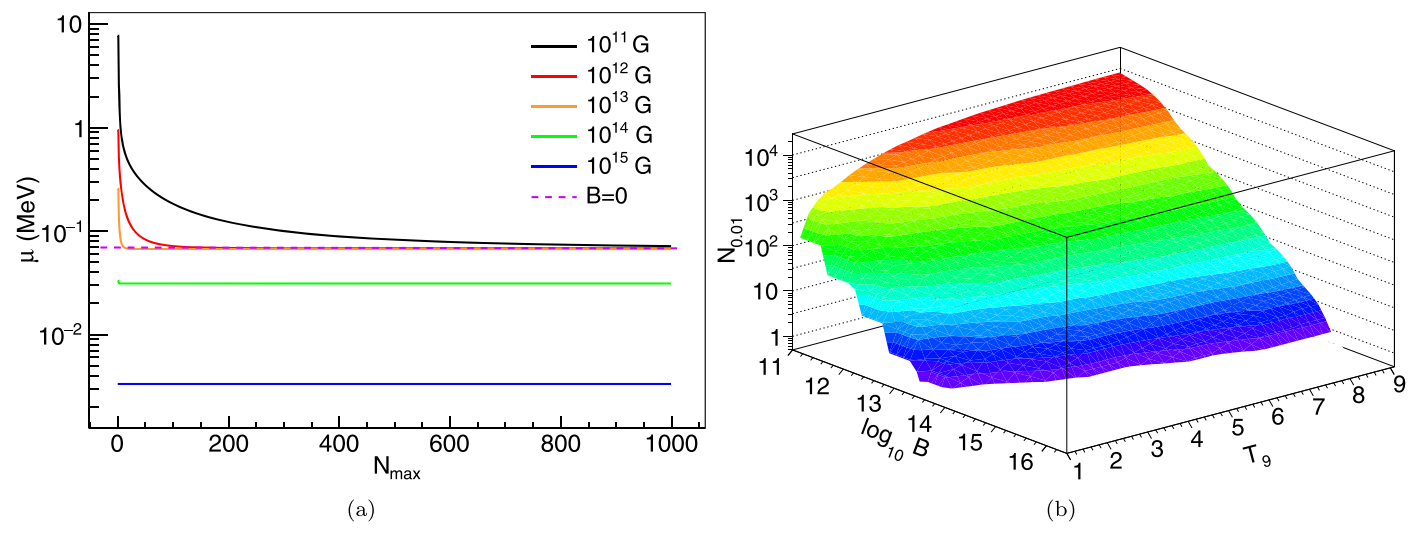


Figure 3. (a) Electron chemical potential as a function of the maximum number of Landau levels included in summation over Landau levels at  $T_9 = 2$ ,  $\rho Y_e = 5 \times 10^4$  g cm<sup>-3</sup> for various magnetic fields. The dashed line is the chemical potential for an ideal Fermi gas. (b) Number of Landau levels necessary to approach an equilibrium electron number density with a maximum uncertainty of 1%,  $N_{0.01}$  at a  $\rho Y_e = 5 \times 10^4$  g cm<sup>-3</sup> as a function of magnetic field (G) and  $T_9$ .

 $10^{15}$  G, the convergence is immediate, and the approximation where only the lowest Landau level (LLL) is considered is valid. For  $10^{14}$  G, the convergence occurs rapidly at  $N_{\rm max}=1$ , and the difference between this approximation and the  $N_{\rm max}=1$  summation is small. At lower fields, a summation over more Landau levels is necessary in order to achieve a reasonable accuracy.

It is also interesting to note that at higher fields, the electron chemical potential is reduced as the level density is adjusted by the presence of Landau levels. At the highest fields, the electron transverse momentum is discrete and increases with field. The energy necessary to fill higher Landau levels is large compared to the thermal energy of the plasma, kT, and electrons are forced into the lowest-energy levels. However, if the field is low enough such that  $\sqrt{eB} \ll kT$ , the chemical potential approaches that of an ideal Fermi gas, and the plasma can be treated as such. In this case, the field can be ignored.

Similarly, in Figure 3(b), truncating the sum over Landau levels at a specific number is explored by examining the number of Landau levels necessary to achieve a desired uncertainty. Shown on the right side of this figure is the number of Landau levels necessary,  $N_{0.01}$ , such that the relative

difference between the sum over  $N_{0.01}$  Landau levels and the equilibrium number density is less than 1%:

$$1 - \frac{\sum_{i=0}^{N_{0.01} - 1} h_i}{\sum_{i=0}^{N_{large}} h_i} < 0.01, \tag{5}$$

where  $h_i$  are individual terms in the number density in Equation (2). That is, the relative difference between the number density if only  $N_{0.01}$  Landau levels are used and if a sufficiently large number of Landau levels is used is less than 0.01. For this figure, the density times the electron fraction is  $\rho Y_e = 5 \times 10^4 \text{ g cm}^{-3}$ . For fields that are high enough,  $B \gtrsim 10^{13}$  G, each successive term in the sum drops by roughly an order of magnitude,  $h_{i+1}/h_i \sim 0.1$ . Here, a value of  $N_{\text{large}}$  of 10<sup>4</sup> is assumed. From the left side of the figure, it is seen that even at low fields, sums up to terms less than 10<sup>4</sup> Landau levels are sufficient to characterize the plasma, indicating a choice of  $N_{\rm large} = 10^4$  to be sufficient. Even at low fields, the last  $\sim 3000$ Landau levels in the sum contribute less than 1% to the total electron-positron number density. For a lower field, it is necessary to include several hundred (or more) Landau levels in the sum for an accurate calculation. For the very high field, however, one can achieve a high accuracy by including only the LLL, known as the "LLL approximation". A discussion of the accuracy and utility of the LLL approximation in evaluating the TF length will be given later.

As can be seen from Figures 1 and 3(a), the effect of the magnetic field becomes negligible roughly below 10<sup>13</sup> G. The electron–positron population is determined almost exclusively by the system temperature and density. In this region, the thermally calculated chemical potential without magnetic fields is almost identical to that computed if magnetic field effects are accounted for and the positron number density approaches zero as stated previously. For the temperature and density used for Figure 3(a), the electron chemical potential if no field were present would be 0.76 MeV. Above 10<sup>13</sup> G, the chemical potential decreases with field.

## 2.2. High-field Approximation: Euler–MacLaurin Formula in Momentum

At high fields and high temperatures, the chemical potential is low, and the electron-positron Fermi distribution is constrained to relatively low momentum. In this case, we consider an Euler-MacLaurin expansion in momentum using the Euler-MacLaurin formula. The net electron number density can be written as:

$$n_e = eB \frac{T}{2\pi^2} \sum_{\tilde{p}, n=0}^{\infty} g_n \left( \frac{2 - \delta_{p0}}{2} \right) \times \frac{\sinh \tilde{\mu}}{\cosh \sqrt{\tilde{p}^2 + \tilde{m}^2 + n\gamma} + \cosh \tilde{\mu}}, \tag{6}$$

where  $\gamma \equiv 2eB/T^2$  and terms with a tilde are divided by T,  $\tilde{x} \equiv x/T$ . These terms are unitless. It is noteworthy that, for the Euler–MacLaurin formula, the higher-order derivatives are zero, meaning that the sum above is complete. In the case of a

strong magnetic field, the LLL approximation yields:

$$n_e = eB \frac{T}{2\pi^2} \sum_{\tilde{p}=0}^{\infty} \left(\frac{2 - \delta_{p0}}{2}\right) \frac{\sinh \tilde{\mu}}{\cosh \sqrt{\tilde{p}^2 + \tilde{m}^2} + \cosh \tilde{\mu}}, \quad (7)$$

resulting in a linear dependence on the external magnetic field.

The Thomas–Fermi screening length in a strong magnetic field is derived as:

$$\frac{1}{\lambda_{\text{TF}}^{2}} = 4\pi e^{2} \frac{\partial n}{\partial \mu}$$

$$= eB \frac{e^{2}}{\pi} \frac{\partial}{\partial \tilde{\mu}} \sum_{n=0}^{\infty} g_{n} \int_{0}^{\infty} \frac{d\tilde{p}}{\exp\left[\sqrt{\tilde{p}^{2} + \tilde{m}^{2} + n\gamma} \mp \tilde{\mu}\right] + 1}$$

$$= eB \frac{e^{2}}{\pi} \sum_{n=0}^{\infty} g_{n} \int_{0}^{\infty} \frac{\partial}{\partial \tilde{\mu}} \frac{d\tilde{p}}{\exp\left[\sqrt{\tilde{p}^{2} + \tilde{m}^{2} + n\gamma} \mp \tilde{\mu}\right] + 1}$$

$$= eB \frac{e^{2}}{\pi} \sum_{n=0}^{\infty} g_{n} \int_{0}^{\infty} \frac{d\tilde{p}}{1 + \cosh\left(\sqrt{\tilde{p}^{2} + \tilde{m}^{2} + n\gamma} \mp \tilde{\mu}\right)},$$
(8)

where the  $\mp$  corresponds to the electron/positron number density, and the sum over both electron and positron densities is implied.

The Euler-MacLaurin formula, expanded in momentum, yields an easily computed form for the integral term above:

$$\frac{1}{\lambda_{\text{TF}}^2} = eB \frac{e^2}{\pi} \sum_{\tilde{p},n=0}^{\infty} g_n \left( \frac{2 - \delta_{p0}}{2} \right) \times \frac{1 + \cosh \tilde{\mu} \cosh \sqrt{\tilde{p}^2 + \tilde{m}^2 + n\gamma}}{(\cosh \tilde{\mu} + \cosh \sqrt{\tilde{p}^2 + \tilde{m}^2 + n\gamma})^2} \tag{9}$$

where the sum over n is a sum over Landau Levels, and the sum over  $\tilde{p} = p/T$  results from the Euler–MacLaurin formula for Equation (8).

One can approximate a sum over several Landau levels and only up to a maximum value of  $\tilde{p}$  in the above equation:

$$\frac{1}{\lambda_{\text{TF}}^2} \propto \sum_{n=0}^{\infty} g_n \left[ \sum_{\tilde{p}=0}^{\infty} \dots \right] \rightarrow \sum_{n=0}^{n_{\text{max}}} g_n \left[ \sum_{\tilde{p}=0}^{\tilde{p}_{\text{max}}} \dots \right] + R_{\tilde{p}}, \tag{10}$$

where  $n_{\text{max}}$  is the highest Landau level included in the sum, and  $\tilde{p}_{\text{max}}$  is the highest term included in the Euler–MacLaurin formula. The remainder induced by truncating the sum is  $R_{\tilde{p}}$ .

At high magnetic field, the electron chemical potential is much smaller than the Landau level spacing. In this case, the sum over  $\tilde{p}$  converges rapidly, and the summation can be truncated to a few terms. For the purposes of computation, the limitation of the sum may be determined to truncate at  $\tilde{p}_{\text{max}}$  where the difference in successive terms is smaller than some uncertainty,  $\varepsilon$ :

$$\frac{f_{\tilde{p}_{\max}} - f_{(\tilde{p}_{\max} - 1)}}{f_{\tilde{p}_{\max}}} < \varepsilon. \tag{11}$$

As an example, the relative error in  $\lambda_{\rm TF}$ ,  $\Delta \lambda/\lambda = 1 - \lambda_{McL}/\lambda_{\rm exact}$  (where the Thomas–Fermi length deduced from the truncated sum is  $\lambda_{McL}$  and that deduced from Equation (8) is  $\lambda_{\rm exact}$ ) induced by truncating the Euler–MacLaurin sum to a maximum index of  $\tilde{p}_{\rm max}$  is shown in Figure 4 for temperatures  $T_9 = 7$  and 2, at  $\rho Y_e = 5 \times 10^4 \, {\rm g \, cm}^{-3}$ , and three values of the external magnetic field.

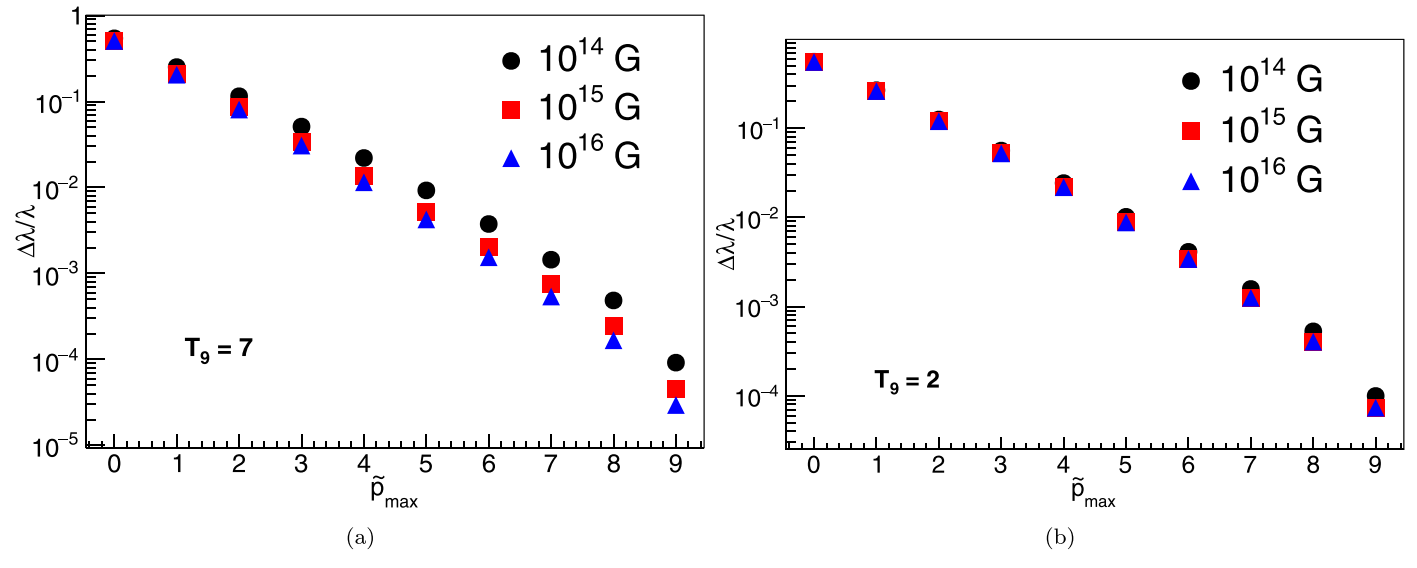


Figure 4. Relative error in the Euler–MacLaurin formula compared to exact numerical computation for the integration in Equation (8) as a function of maximum  $\tilde{p}$  in the sum. Computations are for  $\rho Y_e = 5 \times 10^4$  g cm<sup>3</sup> at temperatures (a)  $T_9 = 7$  and (b)  $T_9 = 2$ . The maximum Landau level calculated in each case is  $N_{\text{max}} = 2000$ .

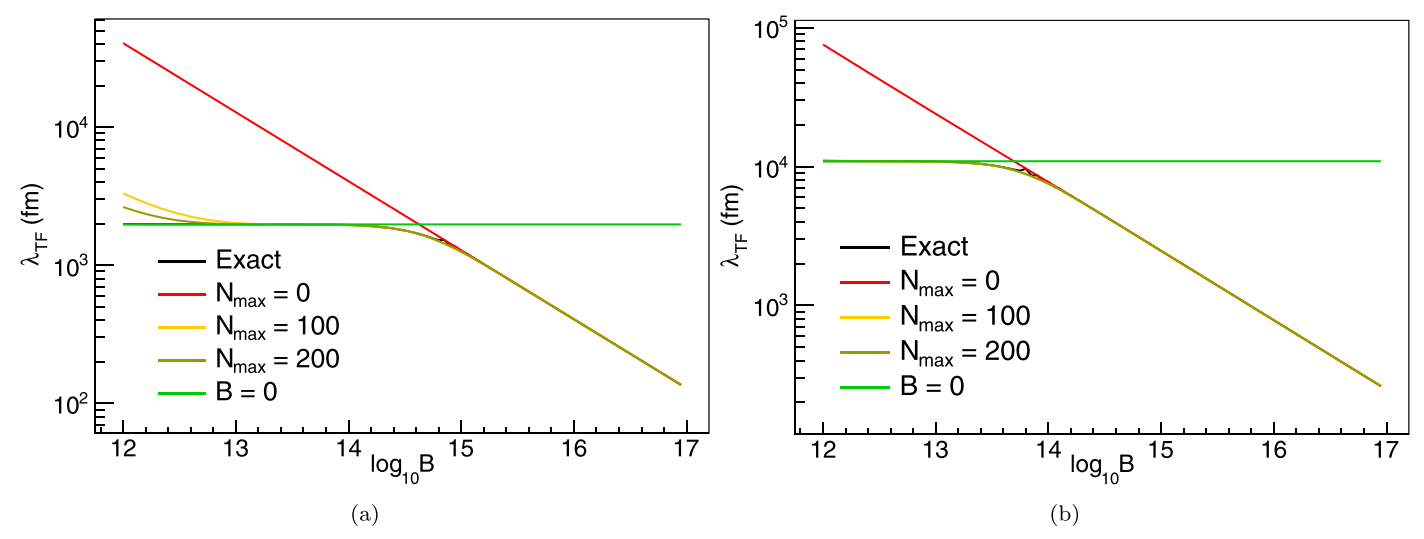


Figure 5. Electron Thomas–Fermi screening length using the approximation described in Section 2.2 for sums up to various maximum Landau levels. In both panels,  $\rho Y_e = 5 \times 10^4 \text{ g cm}^{-3}$ . The temperature is (a)  $T_9 = 7$  and (b)  $T_9 = 2$ . For panel (b), the lines corresponding to  $t_9 = 100$  and  $t_9 = 100$  lie on top of each other. In both panels, only the lowest 12 terms in the Euler–MacLaurin sum are computed,  $\tilde{p}_{max} = 12$ .

Even for a low value of  $\tilde{p}_{\text{max}} = 5$ , the uncertainty is less than 1%.

The validity of this approximation in determining the screening length at temperatures  $T_9 = 2$  and 7 at  $\rho Y_e = 5 \times 10^4 \, \mathrm{g \, cm^{-3}}$  is shown in Figure 5. In this figure, the approximation given in Equation (9) is used to determine the TF screening lengths. For each line in the figure, only the lowest 12 terms in the sum over  $\tilde{p}$  are used. That is  $\tilde{p}_{\rm max} = 12$ . The maximum number of Landau levels summed over is indicated for the various results in the figure.

One sees that the LLL  $(N_{\rm max}=0)$  approximation performs quite well at high fields (log(B)  $\gtrsim$  14). At lower fields, more Landau levels must be included in the sum.

For completeness, the dependence of this approximation on temperature and density is shown in Figure 6, which shows the relative error in the TF length computed with Equation (9) compared to that computed with Equation (8). It can be seen

that—in the weak screening regime—there is almost no dependence on density and a small dependence on temperature. Even at low fields (Figure 6(b)), the error is relatively small. At lower temperatures, the error is somewhat larger. However, this area would very likely correspond to nonrelativistic or intermediate screening.

For a lower field of  $B=10^{13}$  G, the approximation of Equation (9) is shown in Figure 6(b), including the lowest 2000 Landau levels ( $N_{\rm max}=2000$ ) and  $\tilde{p}_{\rm max}=12$ . The TF screening length is still fairly well approximated over a wide range of temperatures and densities even at a lower B field if a sufficient number of Landau levels are included in the sum. For most temperatures and densities, the screening length is within about 10% of the actual Thomas–Fermi length. However, it should also be noted that if the field is low enough,  $\lambda_{\rm TF}$  for B=0 is an excellent approximation, and the effect of the field can be ignored.

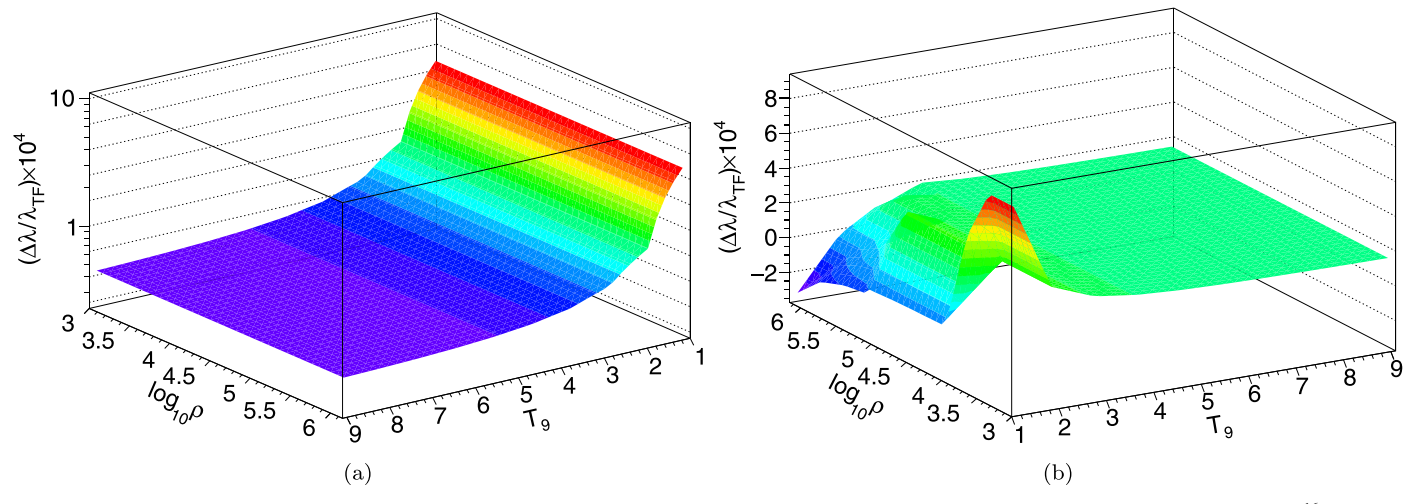


Figure 6. Relative difference in TF screening length Euler–MacLaurin approximation to the exact computation as a function of T and  $\rho$  for (a)  $B = 10^{16}$  G and (b)  $B = 10^{13}$  G for various temperatures and densities. Here, only the LLL approximation is used for the  $10^{16}$  G case, and the lowest 2000 Landau levels are used for the  $10^{13}$  G case. In both panels,  $Y_e = 0.5$ .

### 3. Weak Interactions

In addition to the inclusion of magnetized plasma effects on screening of the Coulomb potential and modifications to the electron–positron chemical potential, effects on weak interaction rates have also been examined. Weak interactions can be altered by changes to the electron Fermi–Dirac distribution function and the electron energy spectrum in weak decays (Fassio-Canuto 1969; Grasso & Rubinstein 2001; Luo et al. 2020). In addition, the shifts to the electron–positron chemical potentials in the thermal plasma are also modified. The shift in chemical potentials can change the Fermi–Dirac functions, altering the available states for capture and decay as well as the Pauli blocking factors. This can influence all of the weak interactions. Also, the electrons and positrons involved in weak interactions are constrained to Landau levels, creating nearly discrete energy spectra, especially at high fields.

In the presence of magnetic fields, the phase space  $(d^3p)$  of the interactions is changed by the presence of Landau Levels. The density of states is (in natural units):

$$dn \propto \frac{d^3p}{(2\pi)^3} = \sum_{n=0}^{\infty} (2 - \delta_{n0}) \frac{eB}{2\pi^2} dp_z.$$
 (12)

The corresponding shift in the lepton energy spectra can have dramatic effects on the weak interaction rates in a magnetized plasma. With the inclusion of density distributions modified by the existence of Landau levels, the approximate weak interaction rates can be rewritten with the momentum component parallel to the magnetic field vector and the discrete transverse momentum components (Fassio-Canuto 1969; Grasso & Rubinstein 2001; Luo et al. 2020):

$$\Gamma_{\beta^{-}} = \kappa \frac{eB}{2} \sum_{n=0}^{N_{\text{max}}} (2 - \delta_{n0}) \int_{\omega_{\beta}}^{Q} \frac{E(Q - E)^{2}}{\sqrt{E^{2} - m_{e}^{2} - 2neB}} \times (1 - f_{FD}(E, \mu_{e})) (1 - f_{FD}(Q - E, -\mu_{\nu})) dE, \quad (13)$$

$$\Gamma_{\beta^{+}} = \kappa \frac{eB}{2} \sum_{n=0}^{N_{\text{max}}} (2 - \delta_{n0}) \int_{\omega_{\beta}}^{-Q} \frac{E(-Q - E)^{2}}{\sqrt{E^{2} - m_{e}^{2} - 2neB}} \times (1 - f_{FD}(E, -\mu_{e})) (1 - f_{FD}(-Q - E, -\mu_{\nu})) dE, \quad (14)$$

$$\Gamma_{EC} = \kappa \frac{eB}{2} \sum_{n=0}^{N_{\text{max}}} (2 - \delta_{n0}) \int_{\omega_{EC}}^{\infty} \frac{E(E - Q)^2}{\sqrt{E^2 - m_e^2 - 2neB}} \times f_{FD}(E, \mu_e) (1 - f_{FD}(E - Q, \mu_{\nu})) dE,$$
 (15)

$$\Gamma_{PC} = \kappa \frac{eB}{2} \sum_{n=0}^{N_{\text{max}}} (2 - \delta_{n0}) \int_{\omega_{PC}}^{\infty} \frac{E(E+Q)^2}{\sqrt{E^2 - m_e^2 - 2neB}} \times f_{FD}(E, -\mu_e) (1 - f_{FD}(E+Q, -\mu_{\nu})) dE,$$
 (16)

where the following quantities are defined (Hardy & Towner 2009; Arcones et al. 2010):

$$\omega_{EC/PC} \equiv \max[\pm Q, m_e],$$

$$\omega_{\beta} \equiv \sqrt{m_e^2 + 2neB},$$

$$N_{\max} \leqslant \frac{Q^2 - m_e^2}{2eB},$$

$$\kappa \equiv \frac{B \ln 2}{Km_e^5},$$

$$B \equiv 1 + 3g_A^2 = \begin{cases} 5.76, & \text{nucleons}, \\ 4.6, & \text{nuclei}, \end{cases}$$

$$K \equiv \frac{2\pi^3 \hbar^7 \ln 2}{G_e^2 m^5} = 6144 \text{ s.}$$
(17)

Here the transition Q value is the difference in nuclear masses.

In Equations (13)–(16), the Fermi–Dirac distributions are cast to accommodate the electron energy of individual Landau levels. The energy distribution of an electron in the nth Landau level is:

$$f_{FD}(E, \mu_e) = \frac{1}{\exp\left[\frac{\sqrt{E^2 + 2neB} - \mu_e}{T}\right] + 1}.$$
 (18)

For positrons, the chemical potential is negative.

Unlike the case of an ideal Fermi gas, the electron–positron energy spectrum in weak interactions is not thermal, and the LLL approximation is not necessarily applicable. For example, the evolution with magnetic field of the  $\beta^-$  spectrum for a nucleus with a decay Q value of 12 MeV at  $T_9=2$  and  $\rho Y_e=500~{\rm g~cm}^{-3}$  is shown in Figure 7. This spectrum is the

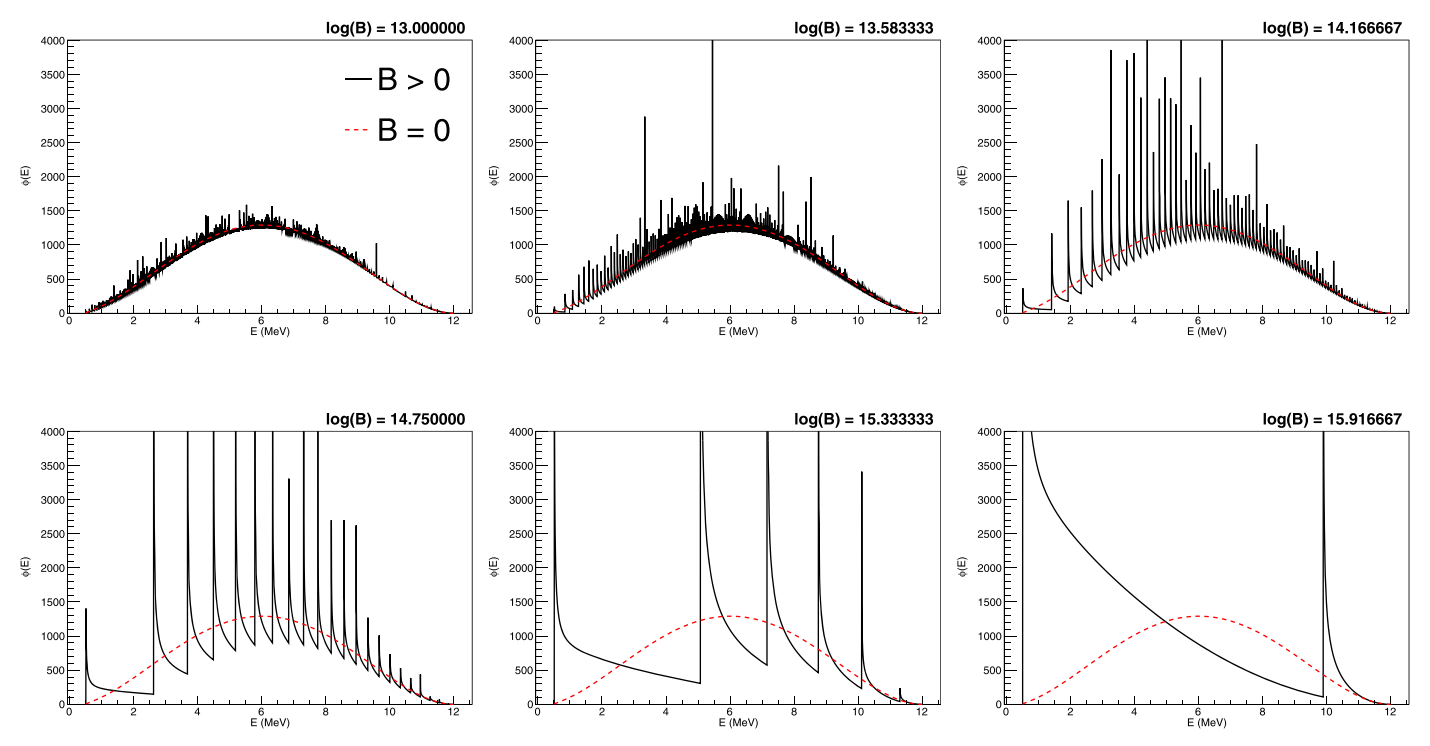


Figure 7. Evolution of the  $\beta^-$ -decay spectrum with magnetic field for six different fields indicated in each panel. The red dashed line indicates the spectrum for B=0, and the black line indicates the spectrum for the magnetic field indicated in each figure. For this series of figures, the decay Q value is 12 MeV, and the values of  $T_9$  and  $\rho Y_e$  are 2 and 500 g cm<sup>-3</sup>, respectively. The magnetic field units are G.

integrand of Equation (13). In the case of a nonzero field, the  $\beta$  spectrum is a sum of individual spectra for each Landau level with the maximum Landau level energy less than the decay Q value,  $\sqrt{2neB + m_e^2} \leqslant Q$ .

For a lower field, the Landau level spacing is much less than the Q value of the decay  $\sqrt{eB} \ll Q$ . An electron can be emitted into any of a large number of Landau levels with level energies less than the electron energy. The Landau level spacing is quite small in this case. For decays to many possible Landau levels, the integrated spectrum is closer in value to the zero-field spectrum. In other words, as  $eB \to 0$ , the integrated nonzero-field spectrum approaches the zero-field spectrum. The sum in Equation (13) becomes an integral, and the Landau level spacing  $eB = \Delta p^2 \to d^2p$ . The sum over all Landau levels approaches the zero-field spectrum.

As the magnetic field increases, such that  $\sqrt{2neB} \sim Q$ , fewer Landau levels contribute to the total spectrum. For a very few levels, the zero-field and nonzero-field spectra can be dramatically different, and the decay rates can be magnified for higher fields.

This could be potentially important for an r-process that proceeds in a high magnetic field, such as in a collapsar jet or NS merger, for example. Because the r-process encompasses nuclei with a wide range of  $\beta^-$  decay Q values, the effects of an external magnetic field can be significant. This is shown in Figure 8, which shows the electron energy spectrum in  $\beta^-$  decay for several cases of Q value and magnetic fields. This spectrum is also the integrand of Equation (13). Spectra are computed for  $\beta^-$  decays at  $T_9 = 2$  and  $\rho Y_e = 500 \,\mathrm{g \, cm^{-3}}$ .

In this figure, four cases are shown for each combination of two Q values of 3 and 12 MeV and two cases of magnetic field of  $10^{15}$  G and  $10^{16}$  G. For the low Q value of 3 MeV, the electrons can only be emitted into the LLL for both fields, and the sum in Equation (12) consists of only the n = 0 term;

 $N_{\rm max}=0$ . However, at a higher Q value of 12 MeV, the electron can be emitted into any of a number of Landau levels. For example, an electron emitted with an energy of 6 MeV could fall into the N=0, 1, or 2 Landau level. The integration is thus a sum over all Landau levels up to the maximum possible Landau level within the  $\beta$  spectrum;  $N_{\rm max}=11$  in this case. For a field of  $10^{15}$  G, the Landau level spacing  $\sqrt{eB}=2.43$  MeV, which is less than the decay Q value, so multiple Landau levels contribute to the  $\beta$  spectrum.

For a higher field of  $10^{16}$  G, with a Landau level spacing of 7.69 MeV, even at high  $\beta^-$  decay Q values, only a few (or one) Landau levels can be occupied by the emitted electrons. Further, as indicated in Figure 8, for decay spectra that occupy very few Landau levels, the integrated spectrum, which is proportional to the total decay rate, can be significantly higher than the zero-field spectrum.

The relationship between the Landau level spacing and the  $\beta$ -decay Q value is important in considering the astrophysical r-process. Because the r-process proceeds along a path of potentially very neutron-rich nuclei, the  $\beta^-$  decay Q values can be quite large,  $\sim \! 10$  MeV. Thus, for an r-process in a high-field environment, the decay rates could be quite sensitive to the field. However, because the Q values are large, one cannot necessarily assume that the decay rates can be computed with just the LLL approximation.

The influence of high magnetic fields on  $\beta^-$  decay is shown in Figure 9 for two assumptions of the magnetic field and two assumptions of Landau levels (whether the LLL approximation is used or not) at a temperature  $T_9=2$  and  $\rho Y_e=500$ . Here, the ratios of decay rates in a nonzero field to those in a zero field  $\Gamma(B\neq 0)/\Gamma(B=0)$  are plotted for each  $\beta^-$  unstable nucleus with Q values taken from the AME2016 evaluation (Wang et al. 2017).

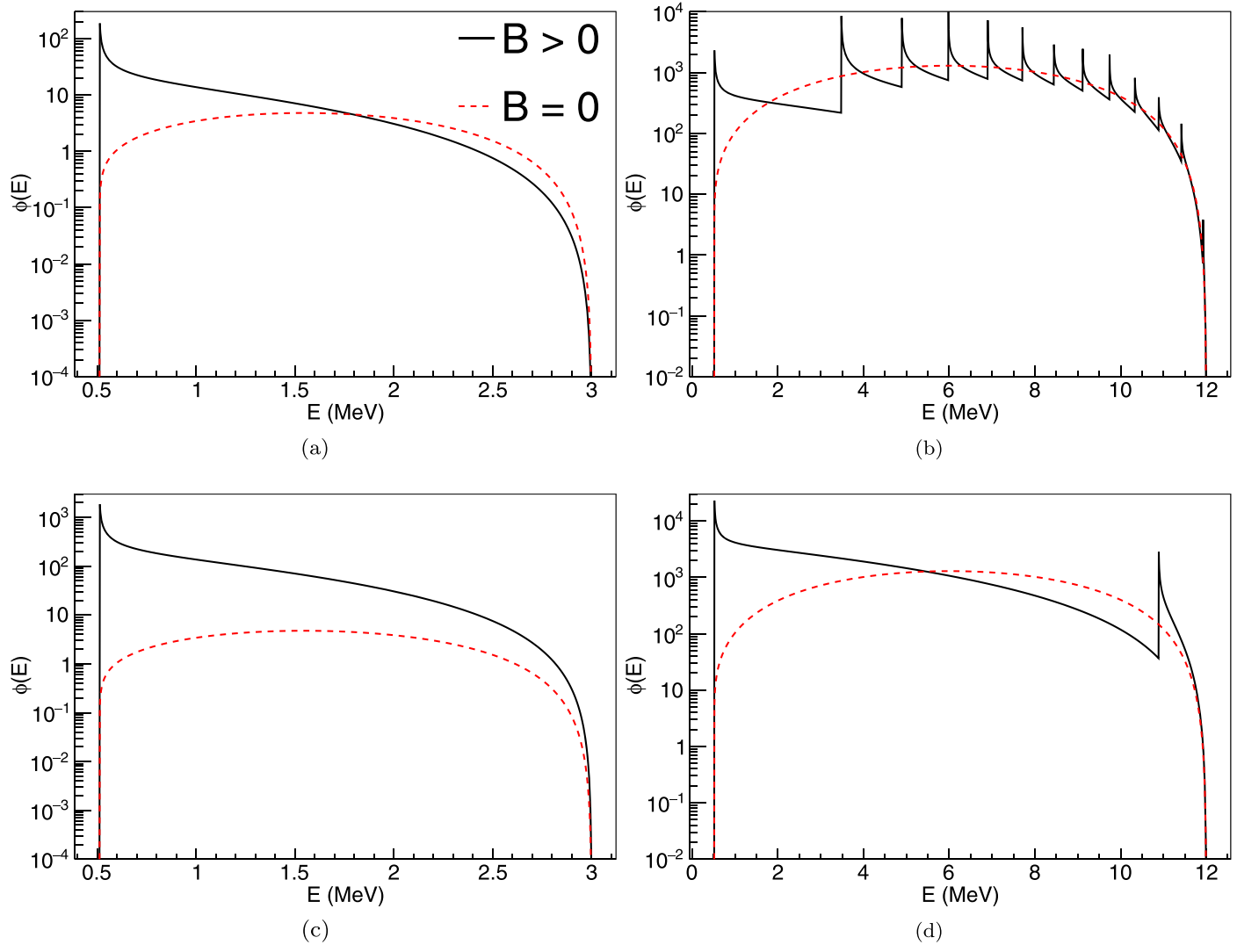


Figure 8. Electron  $\beta$ -decay spectra for  $B=10^{15}$  G (a), (b) and  $10^{16}$  G (c), (d) for low Q values (a), (c) and high Q values (b), (d). The spectra are calculated at  $T_9=2$  and  $\rho Y_e=500$  g cm<sup>-3</sup>. The red dashed lines correspond to the spectra for B=0.

Several findings are noted in this figure. First, for nuclei closer to stability, the Q values are much lower, and the rate ratio is higher. This is because electrons are emitted in only a few (or one) Landau levels. These nuclei would correspond to the schematic cases of Figures 8(a) and (c).

For the higher field of  $10^{16}$  G, the figures for the LLL assumption and the assumption for all relevant Landau levels are very similar, indicating that the LLL is the primary contributor to the electron spectra in  $\beta^-$  decay for all nuclei at this field strength. At this field, the difference between the zero-field and nonzero-field computations is significant, and the increase in rates is much higher. However, for a field of  $10^{15}$  G, inclusion of only the LLL underestimates the total rate. Including all relevant Landau levels in the rate computation is necessary.

For more neutron-rich nuclei, more Landau levels are filled by the emitted electron, and the  $\beta$  spectrum more closely matches the zero-field spectrum. Thus, the ratio approaches unity. This would correspond to the case represented schematically in Figure 8(b).

For a higher field, the ratio is close to unity only for the most neutron-rich nuclei, where the Q values are high enough fill

multiple Landau levels in the decay. For the nuclei closer to stability, the Q values are low enough that only a single Landau level is filled by the ejected electron, resulting in a decay spectrum that is significantly different than the zero-field case. For the  $B=10^{16}$  G case for nuclei close to stability, the larger rates would correspond to the decay spectrum represented schematically in Figure 8(c).

# 4. Effects of External Magnetic Fields in r-process Nucleosynthesis

As an example, r-process nucleosynthesis in a collapsar jet trajectory is examined. It is thought that the magnetic fields associated with collapsar jets and neutron star mergers (NSMs) could be as high as  $10^{16}$  G (Takiwaki et al. 2009; Kiuchi et al. 2014, 2015; Nakamura et al. 2015). Such strong fields are formed by amplifying initially weak fields associated with the accretion region. While these fields may be near the surface of the objects, these will be considered as a possible upper limit in nucleosynthesis associated with collapsars and NSMs. Within the actual jet region in this model, fields have been computed to be  $\sim 10^{12-14}$  G (Harikae et al. 2009). Other evaluations of

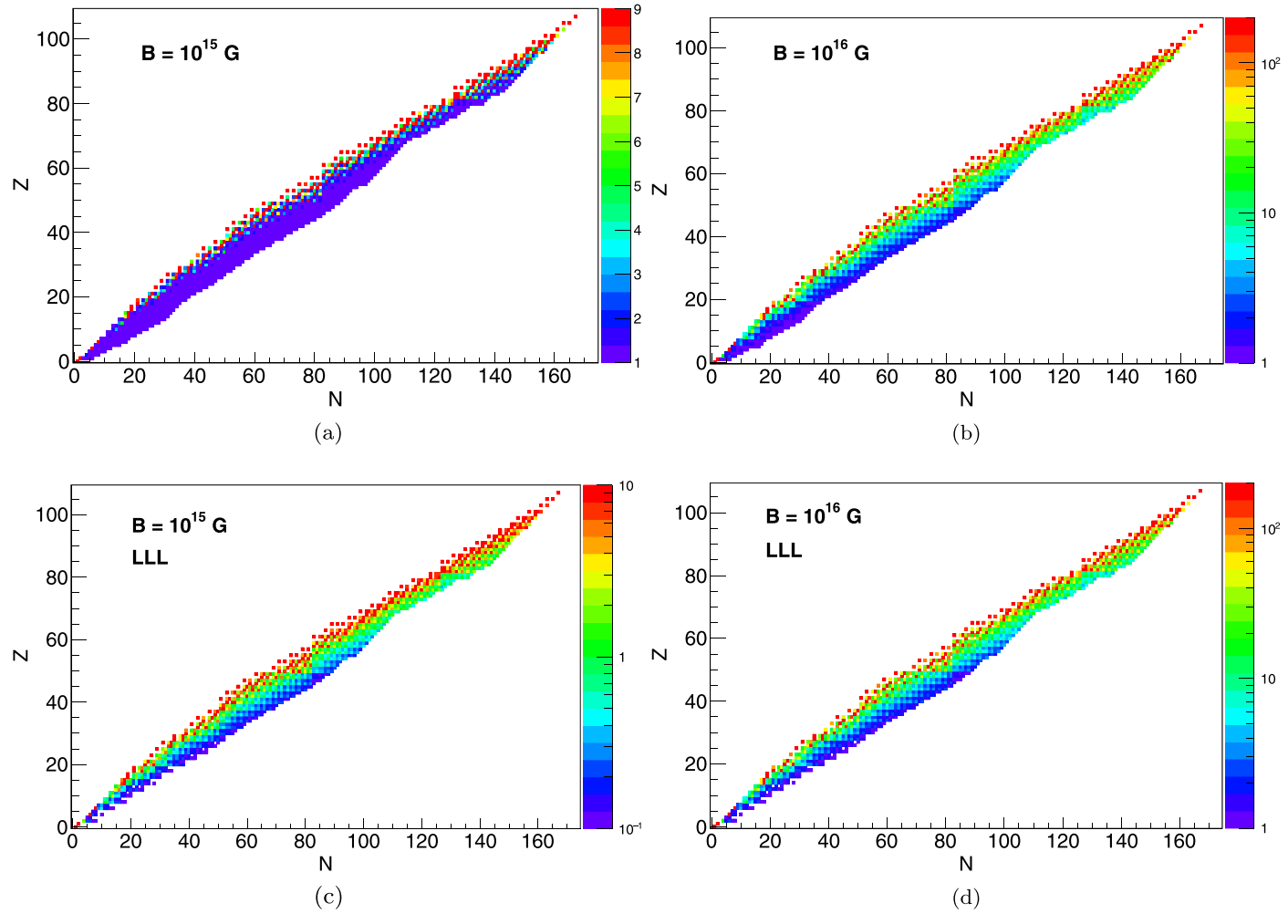


Figure 9. Ratio of  $\beta^-$  decay rates for decay of nuclei unstable against  $\beta^-$  decay in a nonzero field to those in a zero field,  $\Gamma(B \neq 0)/\Gamma(B = 0)$  for magnetic fields  $B = 10^{15}$  G (a), (c) and  $B = 10^{16}$  G (b), (d). The top row corresponds to ratios for which all relevant Landau levels are included in the decay calculation, while the bottom row is for calculations for which only the lowest Landau level is included in the calculations. In all figures,  $T_9 = 2$ ,  $\rho Y_e = 500$  g cm<sup>-3</sup>. Note the difference in scales in each figure.

magnetic fields in collapsars or NSMs have resulted in similar fields near the surface or the accretion disk, with some estimates up to and exceeding 10<sup>17</sup> G (Price & Rosswog 2006; Ruiz et al. 2020). While the field in the actual nucleosynthesis site may vary significantly, a few field cases are examined here to show the field magnitudes necessary to result in significant differences in the final r-process abundance distribution. Some of the fields investigated in the r-process nucleosynthesis studied here may very well exceed realistic values or those in nature and are thus illustrative in conveying field-strength effects in nucleosynthesis processes. Temperature effects, on the other hand are computed for the actual environmental temperature of the r-process site. Here, the effects of Coulomb screening in the early stages of the r-process as well as the effects from the enhancement of weak interaction rates by the external field are examined.

Several nucleosynthesis scenarios are investigated to evaluate the effects on r-process nucleosynthesis. These scenarios are listed in Table 1, where the notation  $X(F)_{\log B}$  is used; the label "X" refers to a specific screening and weak interaction treatment at a field B, and "F" indicates the inclusion of fission cycling or not. For example, model  $A_{14}$  is model A at a magnetic field of  $10^{14}$  G without fission cycling, while model

Table 1

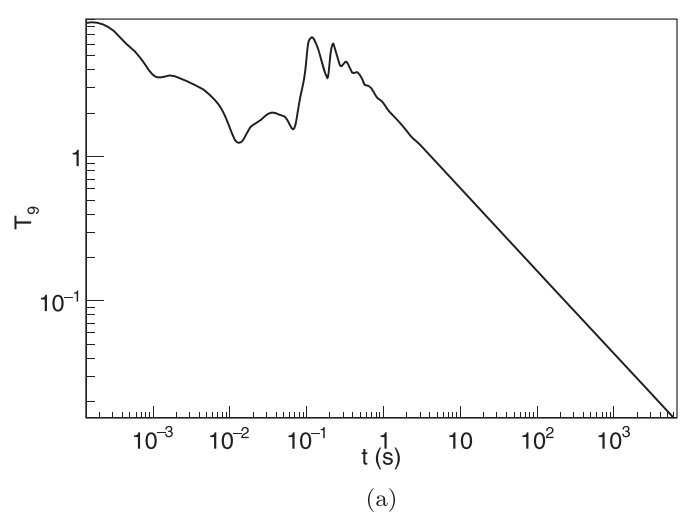
Models Used to Evaluate the Effects of Screening from Temperature and Magnetic Fields as well as Effects from Magnetic Fields on Weak Interactions

Model	Screening	Weak Interactions
$\overline{A(F)_{\log B}}$	None	B=0
$B(F)_{\log B}$	Classical	B = 0
$C(F)_{\log B}$	Relativistic ( $B = 0$ )	B = 0
$D(F)_{\log B}$	Relativistic $(B \neq 0)$	B = 0
$E(F)_{\log B}$	Relativistic $(B \neq 0)$	$B \neq 0$ , LLL only
$F(F)_{\log B}$	Relativistic $(B \neq 0)$	$B \neq 0$ , All LL

Note. For each model, the subscript is the magnetic field strength.

AF<sub>14</sub> is the same model with fission cycling included. The various models summarized are:

- 1. No Coulomb screening and no magnetic field effects, (models  $A_{\log B}$  and  $AF_{\log B}$ ).
- 2. Default classical screening in which weak screening is determined by electrons in a Maxwell distribution (Jancovici 1977; Itoh et al. 1979; models  $B_{\log B}$  and  $BF_{\log B}$ ).



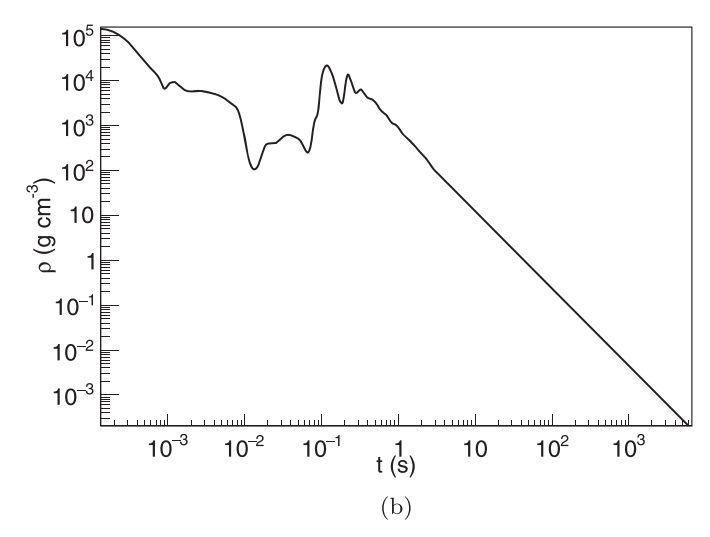


Figure 10. Trajectory used for the MHD r-process nucleosynthesis calculation. (a) Temperatures,  $T_9$ , and (b) density.

- 3. Relativistic screening in which the weak screening TF length is determined from electrons in an ideal Fermi gas (Famiano et al. 2016; models  $C_{log B}$  and  $CF_{log B}$ ).
- 4. Relativistic screening including effects on the TF length from an external magnetic field on the Fermi gas (Luo et al. 2020; models  $D_{\log B}$  and  $DF_{\log B}$ ).
- 5. Relativistic including effects on the TF length plus magnetic field effects on weak interaction rates assuming the LLL approximation, (models  $E_{\log B}$  and  $EF_{\log B}$ ).
- 6. Relativistic including effects on the TF length plus effects on weak interaction rates including all contributing Landau levels to the  $\beta^-$  decays, (models  $F_{\log B}$  and  $FF_{\log B}$ ).

In Table 1, the models indicated by B=0 are those for which the magnetic field effects are not included in the evaluation of screening or weak interactions. Model E includes effects of the magnetic field on weak interactions, but only the LLL approximation is used. Model F includes weak interaction effects for all relevant Landau levels in  $\beta^-$  decays.

In order to evaluate the effects of magnetic fields on screening and weak interactions in a possibly highly magnetized plasma in the r-process, a single trajectory from the MHD jet model of Nakamura et al. (2015) was used. This trajectory is shown in Figure 10. Several values of a static, external magnetic field were evaluated. Because the field may not be well understood in many sites, this evaluation is taken to be qualitative only, as a demonstration of the magnitude of the effects of strong external fields in nucleosynthetic sites. Nucleosynthesis in static fields,  $14 \le \log(B) \le 16$ , was evaluated.

For the r-process calculation, the initial composition was assumed to be of protons and neutrons with  $Y_e=0.05$  as given in Nakamura et al. (2015). The nuclear reaction network code NucnetTools (Meyer & Adams 2007) was modified to include thermodynamic effects and screening effects at high temperature and magnetic fields. The reaction network was a full network that was truncated at Z=98.

The weak interaction rates were computed using the relationships in Equations (13)–(16). These rates are ground-state transitions only. However, the purpose of this initial evaluation is not an evaluation of accurate weak interaction rates, but a description of the effects of strong magnetic fields

on nucleosynthetic processes. If transitions to excited states are included, the rates are expected to be even more sensitive to external fields because of the smaller transition Q value relative to the Landau level spacing (Figure 8). Transitions from excited states, on the other hand, may be less sensitive as the Q values are larger, though one must also account for changes in transition order when including excited states.

The nucleosynthesis was computed to 6000 s. In order to do this, an extrapolation of the Nakamura et al. (2012) trajectories to low T and low  $\rho$  was made because the published trajectories stop at 2.8 s. At low-enough temperatures and densities, neutron captures decline, and only  $\beta$ -decays and subsequent smoothing ensues. The temperature and density extrapolation was done assuming an adiabatic expansion for t>2.8 s,  $\log(T_9) \propto \log(\rho) \propto \log(t)$ . This extrapolation allows the temperature and density to drop significantly to follow the processing further in time while examining effects from late-time fission cycling. Clearly, there is still some nucleosynthesis during this phase, and this is used to evaluate long-term effects of the nucleosynthesis.

To include screening effects, relativistic weak screening was used for  $T_9>0.3$ . For lower temperatures, the classical Debye–Hückel screening was used in models C–F (see Figure 2). In model B, classical Debye–Hückel screening was used for all temperatures. For the strong magnetic field, the Thomas–Fermi length of Equation (9) was used. For weaker fields, the difference between the screening lengths for the relativistic case at B=0 and at  $B\neq 0$  is negligible as shown in Figure 5. Thus, to improve the speed of the network calculations, the LLL approximation was assumed with the expansion of Equation (9). In order to determine whether to use the LLL approximation or the thermal screening length (with B=0), the inverse screening length,  $k \propto 1/\lambda$ , was computed in each case, and the maximum value was used:

$$k \to \max[k(B=0), k(B \neq 0)].$$
 (19)

The resultant corresponding screening length was then determined by Equation (9) at high fields and the relativistic length computed in prior work (Famiano et al. 2016) at lower fields. Certainly, there is a small transition region between the low-field and the high-field values shown in Figure 5 where the screening length is overestimated slightly. In this region, the

 Table 2

 Fission Parameters Used in This Evaluation

Parameter	Description	Value
$\overline{W_i}$	Intermediate fragment probability	0.2
$W_{H/L}$	Heavy/Light fragment probability	0.4
$N_{\rm loss}$	Average neutrons/fission	2
$\sigma$	Width of fragment distribution	7
$\alpha$	Relative difference of centroids of fragment distributions	0.18

Note. Fission model taken from Shibagaki et al. (2016).

screening length could be overestimated by as much at  $\sim 15\%$ , with a resultant shift in the overall reaction rates of about 15%. This can be corrected by relaxing the LLL approximation and including as few as 10 Landau levels in the length calculation. However, it is ignored in this evaluation because the correction is small compared to the change in screening length from the magnetic field. The r-process is not expected to be dominated by screening as it is primarily a neutron capture process, and the time spent in this transition region for the r-process is expected to be brief compared to the entire r-process. Future, more accurate evaluations may include this small correction.

Effects from fission cycling were included in a rudimentary fashion following the prescription of Shibagaki et al. (2016). In this model, fission was implemented for the Cf isotopic chain, <sup>270–295</sup>Cf. Fission rates were assumed to be 100 s<sup>-1</sup> for all nuclei in this isotopic chain. The fission parameters in the Shibagaki et al. (2016) model are shown in Table 2. With this parameter set, the fission distribution for <sup>282</sup>Cf is shown in Figure 11. Clearly, this fission model is overly simplistic and does not represent the full details of the nuclear structure necessary for a proper determination of fission. However, as we will discuss later, it is necessary to include fission in a collapsar/NSM r-process, and this model provides an appropriate level of detail to capture the overall effects of intense magnetic fields on  $\beta$  decays in this site. Fission of the Cf isotopic chain here is meant to replace neutron-induced fission,  $\beta$ -delayed fission, and spontaneous fission of all fissile nuclei produced in the r-process path. As such, the fission product distribution can be contrasted with that developed using more accurate models. For example, the evaluation of fission using the GEF 2016 and FREYA models (Vassh et al. 2019) predicts similar neutron emission in fission, though the fission product distribution for the Cf nuclei is generally symmetric for spontaneous fission with asymmetric components for neutroninduced fission. Fission induced by  $\beta$  decay of the Cf chain has been predicted to be predominantly symmetric for N > 180with asymmetric components at lower mass (Kodama & Takahashi 1975; Vassh et al. 2019).

### 4.1. r-process Abundance Distributions

The final abundance distributions for all six models studied with and without fission are shown in Figure 12 for a field of  $10^{15}$  G. Figure 13 shows the final abundance distributions for models including fission at a field of  $10^{14}$  G. (All models except  $E_{14}$  and  $EF_{14}$  are shown in Figure 13.) The electron fraction  $Y_e$  is plotted for all models in Figure 14.

In all cases, Coulomb screening of nuclear reactions has a minimal effect on the overall reaction network. This is not surprising as the primary fusion reaction is neutron capture, which is immune to screening. While the inclusion of magnetic fields creates a slight enhancement in the overall abundance for the heavier nuclei due to the enhancement of charged-particle reactions early in the r-process (e.g., proton and alpha captures), this enhancement is minimal. Likewise, the effects from default screening and relativistic screening are negligible in this treatment.

However, the inclusion of enhanced weak rates does have an effect on the overall resultant reactions. For a full treatment, including accurate computations of the weak rates with contributions from all relevant Landau levels, the overall  $\beta^$ rates are higher, resulting in a more rapid progression to the heaviest nuclei. As can be seen in the case for no fission in Figure 12, the rapid  $\beta$ -decay rates result in a large abundance of nuclei near the endpoint of the reaction network (Z = 98). The nucleosynthesis progresses to the Cf isotopic chain, where the abundance builds up. At this point, the only possible reactions are  $(n, \gamma)$ ,  $(n, \alpha)$ , neutron-induced fission, and photospallation reactions as a result of truncating the network at Z = 98. This results in additional neutron production and minimal production of  $\alpha$  particles. Of course, this is an unrealistic scenario because of the artificial termination point in the nucleosynthesis, but it does convey the increased nucleosynthesis speed from the high magnetic field in a very neutron-rich environment.

The LLL approximation for  $\beta^-$  decay rates is also shown in this figure. In this case, the Landau level spacing is generally less than the decay Q value, except for a few low-mass nuclei with  $Z\lesssim 20$ . This yields overall slower  $\beta$ -decay rates, resulting in a slower progress to the heavy-mass nuclei and a larger relative abundance at the low-mass nuclei.

The right side of Figure 12 shows the final abundance distributions if fission cycling is included in the network calculation. As expected, there is very little difference between the abundance distributions if nuclear screening is included in the reaction network. However, the inclusion of  $\beta^-$  decay enhancement results in an enhancement of the low-mass nuclei,  $(Z,A)\lesssim (40,100)$ . For the heavier-mass nuclei, fission products dominate the abundance distribution. As fission becomes dominant, heavier-mass nuclei are enhanced in abundance relative to that of the low-mass nuclei, and one notices a relative increase in abundance for  $Z\gtrsim 40$  for all models.

However, there is also an enhancement of the abundances of the low-mass nuclei with field-enhanced decay rates relative to the abundances of nuclei without them. This is likely a result of the more rapid progression of the r-process to the fissile nuclei. There are two effects that can be considered in this case. First, from Figure 9, it can be seen that the enhancement of the  $\beta^-$  decay rates is less for lower-mass nuclei than for higher-mass nuclei. While this enhancement is small, it results in a somewhat slower progression of the r-process through these lower-mass progenitors *relative to* the progression through higher-mass nuclei. Thus, a slight buildup of abundance relative to the high-mass nuclei can result. This is particularly noticeable if only the LLL is taken into account. The rate differences are more pronounced, and the enhancement of low-mass nuclear abundance is larger.

To a lesser extent, the neutrons produced in fission can also slightly enhance the production of lower-mass nuclei. It is assumed that two neutrons are produced in each fission in this

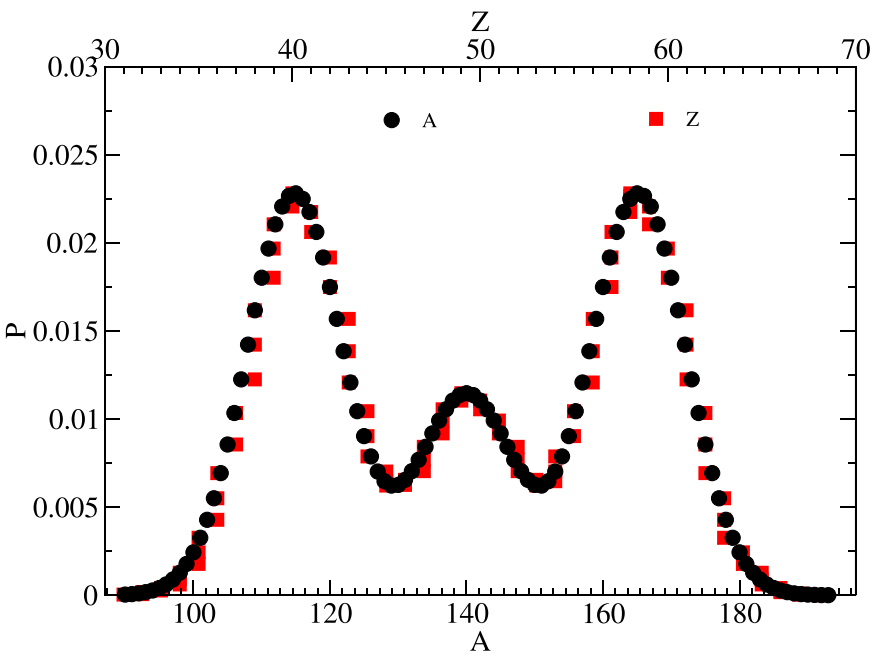


Figure 11. Fission probability distribution in product mass (black circles) and Z (red squares) for  $^{282}$ Cf showing the trimodal structure, which results from a combination of symmetric and asymmetric fission.

model. Because of the very large initial neutron abundance, the progression to fission is not surprising in this scenario. However, for the the case in which decays are enhanced by the magnetic field, the progress to fissile nuclei is more rapid. Thus, more fission neutrons are produced in the r-process. These can be used as fuel for subsequent processing. Of course, neutrons produced in fission are captured by *all* progenitor nuclei, and not just the low-mass nuclei. The slightly lessenhanced decay rates of the low-mass nuclei, on the other hand, result in an abundance that is likely even more enhanced than in the absence of fission.

From Figure 12, one also notes that there is a slight shift to higher mass in the final abundance distribution for the field-enhanced case. This is because the more rapid decay rates result in a slight shift of the r-process path closer to stability than in the case with zero field. This shift is prominent at the abundance peaks. For an r-process path that is closer to stability, the path intersects the magic numbers at a higher mass, resulting in the slight shift by a few mass units. This is shown in the inset for the  $A \sim 195$  abundance peak in Figure 12(b).

Given the prominent contribution to the final abundance distribution by fission, it thus emphasized that—in the collapsar model here—fission cycling is an integral part of r-process calculation.

An evaluation at a field of  $10^{14}$  G is shown in Figure 13. In this figure, the abundances at t = 6000 s for a calculation including fission are shown, and the LLL approximation has been removed for clarity. As expected, for the lower field, the decay rates are closer to the zero-field decay rates, and the overall shift in the abundance distribution is smaller, though a small increase in abundance is noted for A < 100. This trend is consistent with the nonzero-field trends observed but to a lesser extent.

The electron fraction as a function of time,  $Y_e$ , is shown for all six models with and without fission cycling in Figure 14 at a field of  $10^{15}$  G. For each case, it is observed that screening has

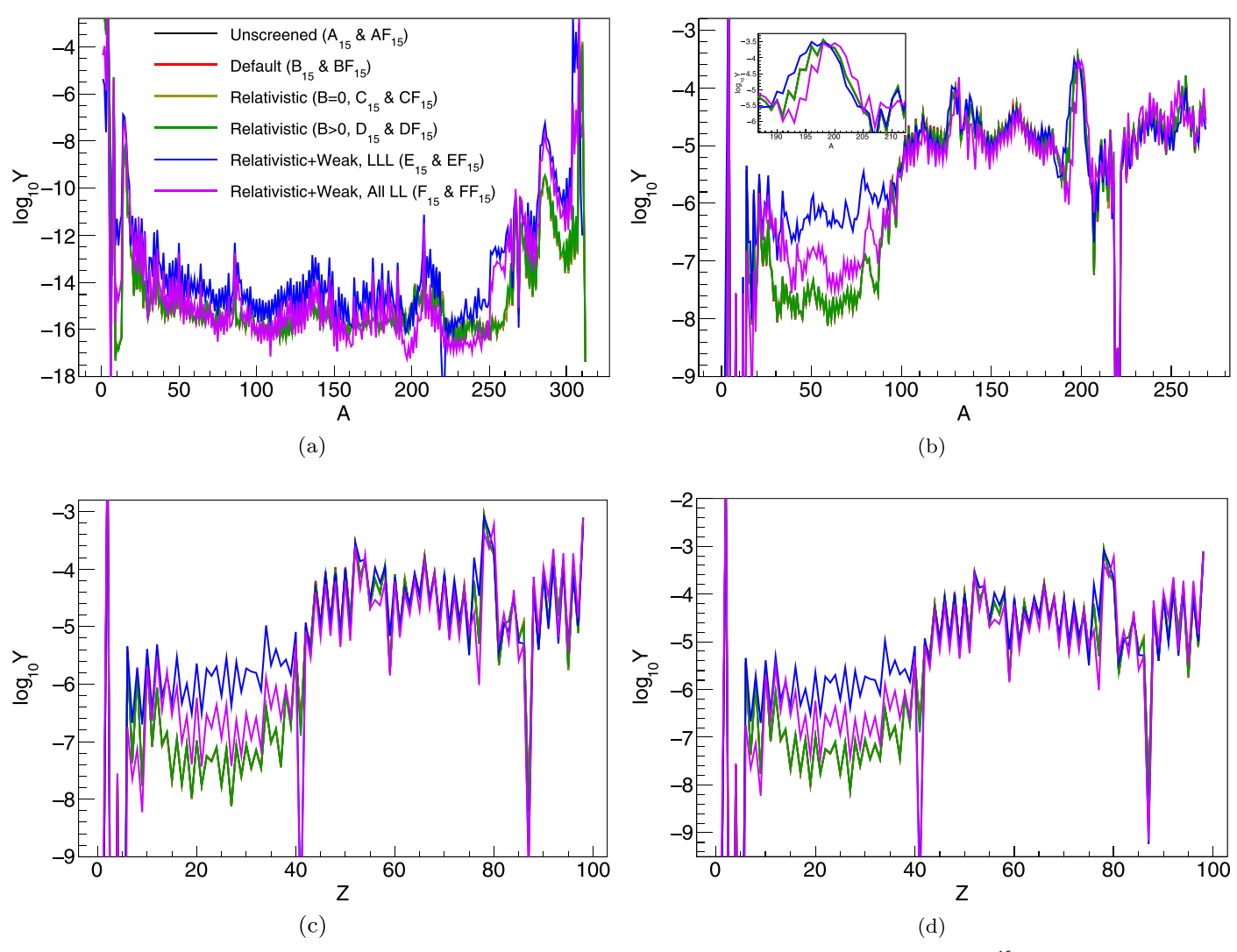
a minimal effect on the evolution of the electron fraction. During the early stages of the r-process, the high-temperature environment is in nuclear statistical equilibrium. As the environment cools and expands, reactions dominate with a small time window during which charged-particle reactions (e.g.,  $(\alpha, \gamma)$ ,  $(\alpha, n)$ , etc.) may occur. These would be affected by Coulomb screening.

Without fission, the dominant contribution to  $Y_e$  is from the Cf isotopic chain. In the case of field-enhanced decay rates, because the progression to the Cf chain is more rapid, an equilibrium  $Y_e$  occurs very rapidly, with a more rapid progression if all Landau levels are included in the decays, as expected. It is also noted that a complete inclusion of all Landau levels results in a slightly higher equilibrium  $Y_e$  as the r-process path is closer to stability. For the other calculations, the  $Y_e$  is lower, as the r-process path is more neutron-rich as explained previously.

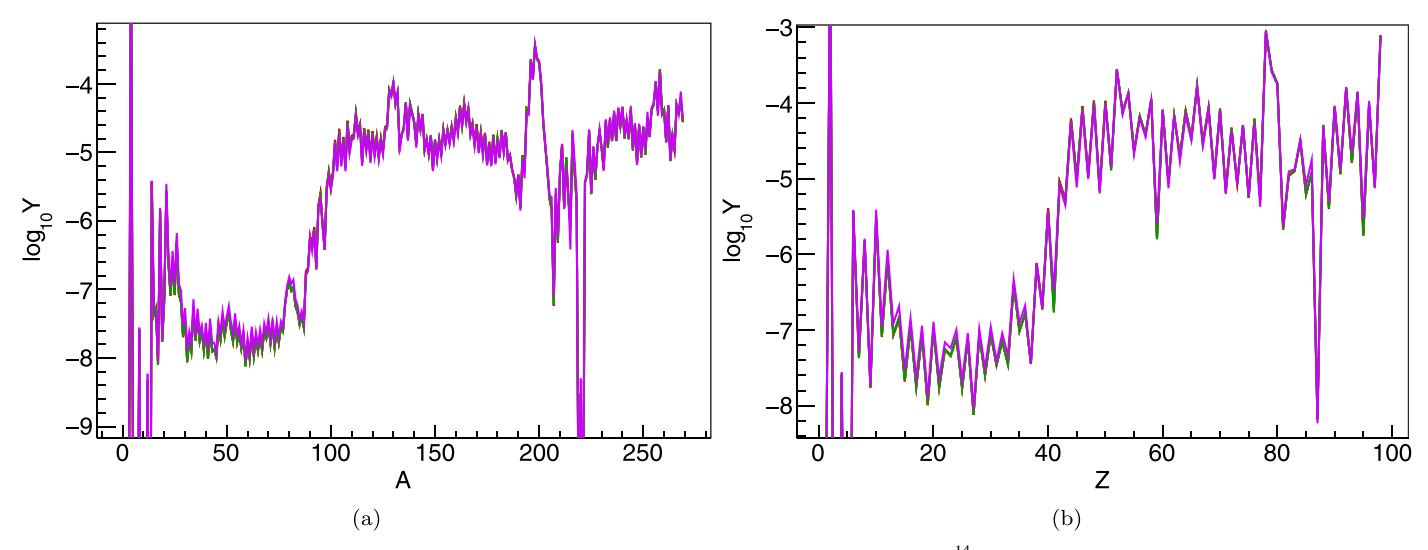
Figure 14(b) shows the evolution of  $Y_e$  in the more realistic case including fission cycling in the calculation. Here, as the r-process becomes dominated by fission products, the equilibrium  $Y_e$  is similar in all cases. However, it can be seen that inclusion of the field-enhanced rates results in an earlier rise in the electron fraction owing to a more rapid r-process combined with a more rapid decay to stability.

#### 4.2. Abundance Ratios

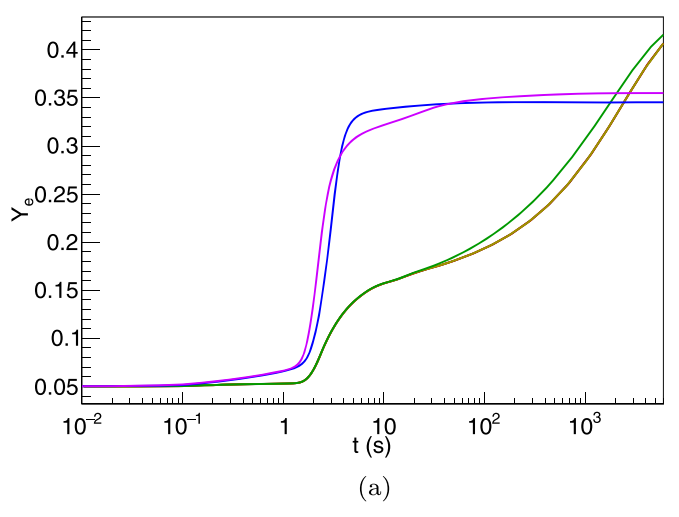
The overall final abundance distribution can be characterized by various abundance ratios. This is particularly helpful in that these provide a characteristic number to gauge the relative contribution from fission compared to the abundance buildup of light nuclei. This ratio is shown for three fields as a function of time in Figure 15 for all six models studied. The zero-field cases are represented by the unscreened and screened relativistic models. The figure shows the abundance ratios for the cases in which fission cycling is accounted for.



**Figure 12.** Abundances at t = 6000 s for MHD models for the adiabatic trajectory in Figure 10 with an external field of  $10^{15}$  G. Panels (a) and (c) show nucleosynthesis results without fission, and panels (b) and (d) show nucleosynthesis results with fission. For the models with fission, the points for the default screening model nearly coincide with those for the unscreened model, and the points for the relativistic screening model for B = 0 nearly coincide with those for the relativistic screening model with  $B = 10^{15}$  G.



**Figure 13.** Abundances at t = 6000 s for MHD models for the adiabatic trajectory in Figure 10 for a field of  $10^{14}$  G including fission. The colors are the same as those in Figure 12. The LLL approximation is not shown.



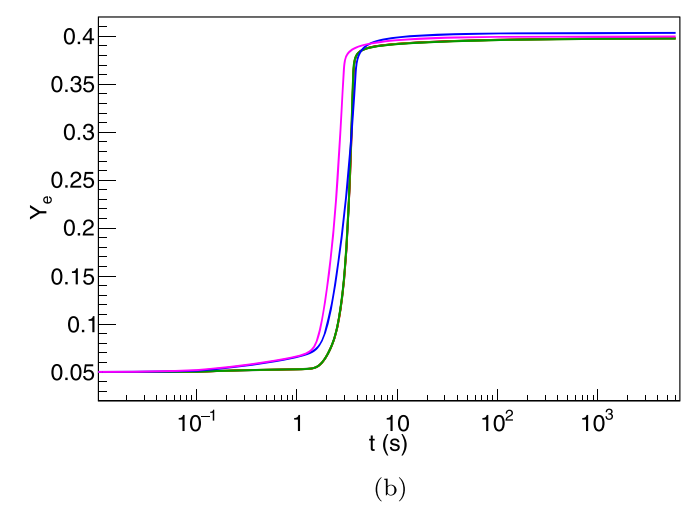


**Figure 14.** Electron fractions as a function of time for trajectories without fission (a) and with fission (b). In both figures the lines for no screening, default screening, and relativistic ( $B = 10^{15}$  G) screening coincide. In the right figure, screening with enhanced weak interactions deviates from the other models. The colors are the same as those shown in Figure 12.

In all cases, the value of the abundance ratio,  $Y_{\rm Sr}/Y_{\rm Dy}$ , drops rapidly as the r-process path moves to the heavier nuclei and into the fissile nuclei, after which an equilibrium abundance of Dy begins to be produced via fission. The abundance ratio continues to drop more gradually with time after  $\sim 4$  s, when the Dy continues to build more slowly, and an equilibrium abundance of Sr is approached. This evolution continues into the post-processing of the r-process. We also notice that the relativistic screening effect—though small—is more prominent than effects from classical screening, resulting in a slight reduction in the Sr/Dy ratio. While this reduction is small compared to effects from the magnetic field on  $\beta$  decays, it can be seen in the figures.

For the lowest field, the effect of the enhanced rates is small because the field-enhanced rates—consisting of decays to many Landau levels—are similar to the non-enhanced rates. If only the LLL approximation is used (model EF<sub>14</sub>), the evolution is significantly different as the rates are grossly underestimated, resulting in a very slow r-process evolution, and the Sr/Dy abundance ratio does not drop until much later in the evolution. For the highest field, on the other hand, there is a smaller difference between the LLL approximation (model EF<sub>16</sub>) and the inclusion of all Landau levels (model FF<sub>16</sub>) in the decay rates because only a few Landau levels are populated in  $\beta$  decays at this field.

Shown in Figure 15(d) are various abundance ratios  $Y_{\rm Sr}/Y_X$  (where X indicates an arbitrary element) at  $t=6000\,{\rm s}$  as a function of the magnetic field. Plotted in the figure is the relative elemental abundance double ratio, R, defined as:

$$R \equiv \frac{(Y_{\rm Sr}/Y_X)_B}{(Y_{\rm Sr}/Y_X)_{B=0}},\tag{20}$$

which shows the evolution of the elemental abundance ratios as the field increases. For low fields, all values are expected to converge at unity as seen in the figure. However, as fields increase, different physical processes affect the ratios.

For the lowest Z element (Te), which can be weakly populated by fission at all fields, a more rapid progression to the fission products can result in a slightly increased production of Te. However, production of Sr via neutron capture is

enhanced by the strong magnetic field. Also, the Sr decay rates are not as enhanced as much as those of Te. Thus the Sr/Te ratio increases with field. For Ba and Dy, however, there is an increase, followed by a decrease. This is because the population of Ba and Dy by fission not only depends on the rate of progression to the fissile nuclei, but also on the final fission distribution. As the r-process path progression to fission for  $B = 10^{15}$  G is similar to that for  $B = 10^{14}$  G (as will be described in the next section), the production of the Ba and Dy progenitors is faster as the field increases up to  $B = 10^{15}$  G. However, above this field, the  $\beta^-$  decay rates are fast enough such that the r-process path itself—being dynamic in nature shifts sufficiently such that the distribution of fissile nuclei changes, and the fission product distribution changes somewhat. One might imagine the peaks of the fission distribution in Figure 11 shifting to lower mass, thus raising or lowering abundances of the progenitors of Ba and Dy. Clearly, the fission model used in this work is too simplistic to make a more than qualitative conclusion, but the interplay between the fission product distribution and the magnetic fields compels further investigation.

The element Tl is also fascinating. It is seen that the Sr/Tl ratio decreases with field. Tl lies above the fission products in mass and Z. However, it also lies just above the A=195 peak in the r-process distribution. Recall from Figure 12 that the r-process distribution shifts slightly to higher mass as the field increases, shifting the A=195 abundance peak as well. This shift, in turn, increases the Tl abundance dramatically, thus reducing the Sr/Tl abundance ratio.

This effect of the magnetic field on the shape of the final r-process abundance distribution, and hence, the  $\mathrm{Sr}/X$  abundance ratio, is compelling, as an r-process from a single collapsar site can be characterized by the abundance distribution, and the magnetic field may be constrained by the abundance ratios. Obviously, a more thorough evaluation incorporating a more realistic fission model is necessary (Beun et al. 2008; Mumpower et al. 2018; Suzuki et al. 2018; Vassh et al. 2019), but the effect on the shape of the abundance distribution can still be made.

While not explicitly evaluated here, it is noted that if magnetic fields as high as  $10^{15}$ – $10^{16}$  G exist in r-process sites,

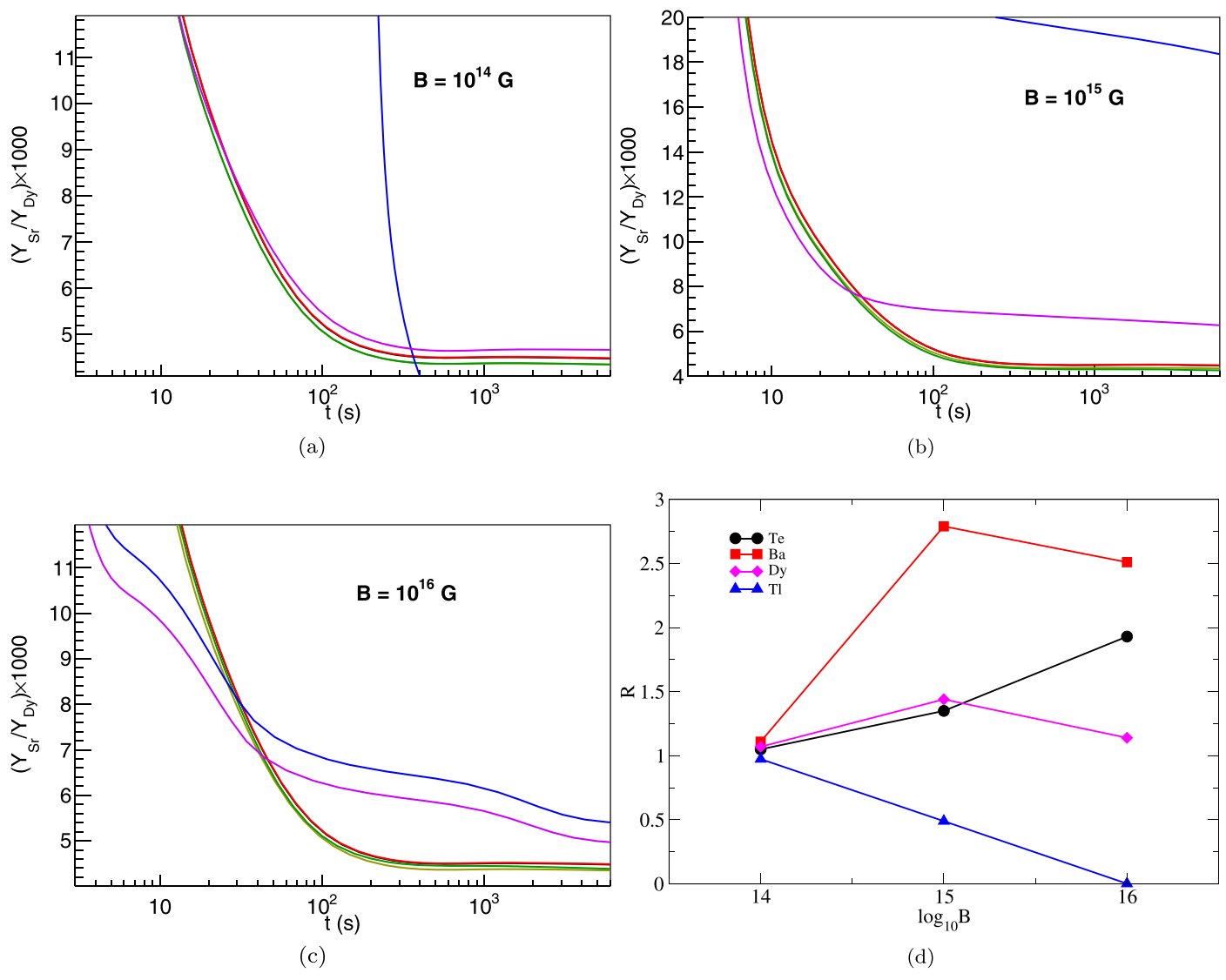


Figure 15. Sr/Dy abundance ratios for the collapsar network calculation for all models in Table 1 for (a)  $B = 10^{14}$  G, (b)  $B = 10^{15}$  G, and (c)  $B = 10^{16}$  G. The colors are the same as those shown in Figure 12. Panel (d) shows abundance double ratios given by Equation (20) for four elements as a function of magnetic field.

neutron capture rates as well as charged-particle reactions may be affected significantly via changes in nuclear distribution functions. The field effect on reaction rates has been studied for one important reaction in Big Bang nucleosynthesis,  $^7\text{Be}(n,p)^7\text{Li}$  (Kawasaki & Kusakabe 2012). That reaction rate is affected only in cases of large magnetic fields, which can be excluded from observations of primordial abundances. However, the field effect through modified distribution functions can potentially change the neutron capture reaction rates with non-flat  $(\sigma v)(E)$  curves at low energies under strong magnetic fields

The ratios studied here may be of particular interest to astronomers in evaluating elemental abundance ratios in stars enriched in single sites. These ratios are generally low compared to solar r-process abundance values (Arlandini et al. 1999) owing to the fact that the single neutron-rich trajectory presented here results in a large abundance of massive elements. The range of observed values from the SAGA database (Suda et al. 2008) is also large compared to the values here. This may likely result from a both a detection limit as well as from the fact that if collapsar jets contribute to the

galactic r-process abundance distribution, they contribute in combination with other sites.

### 4.3. Fission-cycling Time

The fission-cycling time has also been explored, and the effects of a strong magnetic field on the overall fission cycling have been explored from the standpoint of the total time to progress from light nuclei to the fissile nuclei. Naively, one would expect that the fission-cycling time would decrease with magnetic field as the nucleosynthetic progression speeds up.

Here, the fission-cycling time is thought of as the time to progress from the low-mass nuclei in an r-process path to the fissile nuclei. The low-mass nuclei are defined to be those in the Zr isotopic chain (Z=40), and the high-mass nuclei are defined to be those in the fissile region (Z=98). While this is a somewhat arbitrary choice, and while fission cycling is more complex than this, such a method provides a figure-of-merit for the speed at which nuclei can cycle through the r-process to the fissile nuclei.

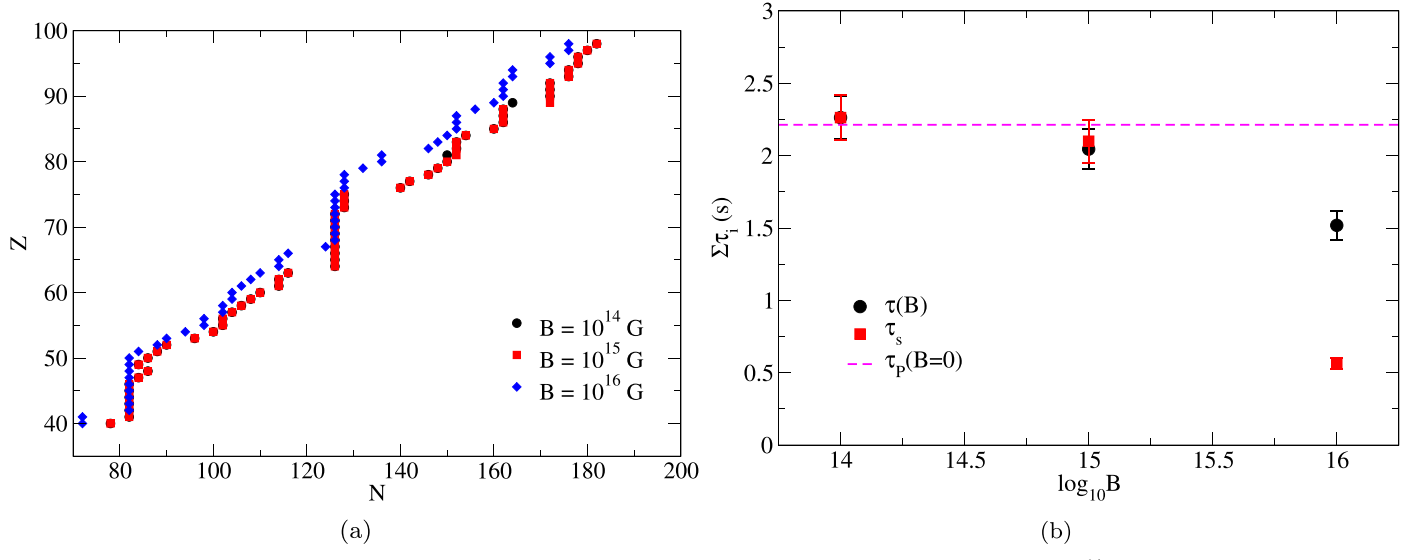


Figure 16. (a) Dynamic r-process paths used to determine fission-cycling times as described in the text. The dynamic path at 10<sup>14</sup> G is also the static path used in this evaluation. (b) Fission-cycling times as a function of magnetic field (in units of G) for the dynamic path, static path, and the zero-field case.

Using the  $\beta^-$  decay lifetimes,  $\tau_{\beta,i}$ , for nuclei along the r-process path, the fission-cycling time,  $\tau_f$ , is then defined as:

$$\tau_f \equiv \sum_{z=40}^{98} \tau_{\beta,z} \tag{21}$$

where the sum is over the most abundant isotope of each element between Zr (Z=40) and Cf (Z=98) along the r-process path at a specific point in time. It then remains to choose a point in time at which the r-process path is chosen. Two methods are utilized to characterize the r-process path.

With the first method, the r-process path is chosen at the point in the evolution when the region containing fissile nuclei is first reached in the r-process. Here, the r-process path is chosen at the epoch when the first Cf nuclei are produced. This is defined to be the point in time when  $Y_{\rm Cf} \geqslant 10^{-20}$ . Because this point depends on the magnetic field, the r-process path at this epoch is unique for each magnetic field. In addition, the temperature and density of the environment are also different at this point, and thus the electron chemical potentials vary in each case. Here, the total fission time is defined by the term  $\tau(B)$ , and the path so-chosen is referred to as the "dynamic" r-process path.

A second method is adopted for comparison. With this method, the r-process path, temperature, and density are chosen to be fixed and independent of the external field; the chosen isotopes are the same for each choice of field. The  $\beta$ -decay lifetimes are then computed for this path as a function of the magnetic field. In this case, the r-process path is chosen to be defined by the isotope with maximum abundance for each element at the point in time when  $Y_{\rm Cf} \geqslant 10^{-20}$  for a specific field of  $10^{14}$  G. At this point in the r-process evolution, the temperature and density are  $T_9{=}1.76$  and  $\rho=377.9~{\rm g~cm}^{-3}$ , respectively. Here, the total lifetime is defined by the term  $\tau_s$ , and the path is referred to as the "static" path.

In order to compute  $\tau(B)$ , the r-process path must then be defined for each field, including a field of  $10^{14}$  G, which is also used to define the r-process path used to compute  $\tau_s$ . The paths defined this way are shown in Figure 16. For fields of  $10^{14}$  G and  $10^{15}$  G, the paths are very similar. The dynamic path corresponding to a field of  $10^{16}$  G is significantly closer to the

valley of stability because of the significantly faster  $\beta$ -decay rates

The computed fission-cycling times are also shown in Figure 16(b) for both definitions of r-process path and for the zero-field case. In either case of the path definition, the fission-cycling time decreases with field. The fission-cycling time for a field of  $10^{14}$  G roughly corresponds to a fission-cycling time with zero field. (There is a small difference due to an imposed decay rate calculation accuracy of 1%, which accounts for the difference in both calculations.) For the static path, the difference is more pronounced at higher fields because the static path is defined to be farther from stability than the dynamic path for the  $10^{16}$  G field. The difference between the static path and the dynamic path case at a field of  $10^{15}$  G is small as the dynamic path at  $10^{15}$  G is very similar to the static path.

It is apparent from this result that fission cycling is faster at higher fields and thus becomes more prominent. The production of fissile nuclei increases during the r-processing time. This results in more fission products, but also an additional neutron abundance in the r-process environment. The initial very low  $Y_e$  in the collapsar model is particularly conducive to producing a significant abundance of fissile nuclei.

### 5. Discussion

Plasma effects on nuclear fusion and weak interactions in hot, highly magnetized plasmas were evaluated, and the example of r-processing in a collapsar MHD jet site was examined. Two primary effects were analyzed. The first is the effect of Coulomb screening on fusion reactions of charged particles. Because the r-process is dominated by neutron captures, screening has a small effect on the overall evolution and final abundance distribution of the r-process. However, charged-particle reactions in the early stages (e.g.,  $(\alpha, n)$  and  $(\alpha, \gamma)$  reactions) may be affected. Coulomb screening is affected by both the temperature and the magnetic field of the environment. While the default classical weak screening commonly used in astrophysics codes was found to have virtually no effect on the final r-process abundance distribution, relativistic effects from high temperatures and high magnetic

fields were found to have a slight effect on the r-process evolution.

The second effect studied is the effect of high magnetic fields on nuclear weak interaction rates. As fields increase in strength, electron momentum transverse to the field direction is quantized into Landau levels. This alters the Fermi-Dirac distribution, resulting in a shift in the electron spectrum. While the magnetic field was found to have a small effect on Coulomb screening, strong fields may have a larger effect on nucleosynthesis when applied to weak interaction rates. This is because—particularly in the case of the finite  $\beta$ -decay spectrum—only a limited number of Landau levels can be occupied by the emitted charged lepton, as indicated in Figures 7 and 8. For very high fields,  $\sqrt{eB} \sim Q$ , only a couple of Landau levels are available to the emitted electron or positron. The electron energy spectra have strong peaks where the electron longitudinal momentum is zero. The integrated spectrum, which is proportional to the decay rate, is thus much larger than that for the zero-field case. Large fields can affect the r-process evolution.

A simple MHD collapsar jet model was adapted from the hydrodynamics calculations of Nakamura et al. (2012) as an illustrative model. In this model, static fields of various strengths were assumed. Various effects of thermal and field effects were studied individually in a systematic manner to gauge the effects of individual environmental parameters. While the temperature was treated dynamically following a single trajectory, which was assumed to decay adiabatically after 2.8 s, the magnetic field in this case was assumed to be constant.

One interesting result of magnetic field effects on the r-process studied was that  $\beta^-$  decay rates increase with field strength. Because of this, the r-process path, which changes dynamically in time, may shift somewhat closer to stability for very strong fields. This has multiple effects. First, the point at which the r-process path crosses the magic numbers changes, thus shifting the abundance peaks of the final distribution. This shape can be evaluated using elemental abundance ratios, such as  $Y_{Sr}/Y_{Tl}$ . Second, the fissile nuclei produced in the r-process will be different, resulting in potentially different fission rates and distributions. This could possibly be studied using abundance ratios such as  $Y_{\rm Sr}/Y_{\rm Ba}$ ,  $Y_{\rm Sr}/Y_{\rm Dv}$ , or something similar. Finally, the fission-cycling time decreases somewhat with increasing field, resulting in an increase in fission products as well as a slight addition of neutrons to the r-process environment.

While the results presented require more precise evaluations, it is interesting to note that—in a highly magnetized r-process site—the elemental abundance ratios can constrain the magnetic field of the site and vice-versa. This might be of interest to astronomers in evaluating stellar abundance ratios in objects thought to contain single-site abundances. The characteristic abundance ratios with an MHD/collapsar model—even at zero field—may characterize the contribution to r-process elements in a star. While the fields presented in this paper are quite large—commensurate with a collapsar, MHD, or possibly NSM—if such fields can be sustained in an r-process site, they would manifest in the isotopic ratios of the site.

Further, it is noted that fission in the collapsar model and effects from the magnetic field may change the contribution to currently observed elements in Galactic chemical evolution (GCE) models. This will be studied in a subsequent paper.

The limitations of the model presented here are noted. These include primarily the static field assumption and the simplified fission model used. If the static field is assumed to be the maximum field in the site, then the results could be thought of as upper limits. Also, the simplified fission model, which was used as the primary evaluation of this paper, exhibited the effects of strong magnetic fields in nucleosynthesis sites. The progenitor nuclei examined in the r-process site in this paper—being quite far from stability—were treated in this much simpler matter. Future work will concentrate on a more thorough treatment of fission in the collapsar/MHD site and its effects on GCE. In addition, a dynamic treatment of the magnetic field will be examined.

M.A.F. is supported by National Science Foundation grant No. PHY-1712832 and by NASA grant No. 80NSSC20K0498. A.B.B. is supported in part by the U.S. National Science Foundation grant No. PHY-1806368. T.K. is supported in part by Grants-in-Aid for Scientific Research of JSPS (17K05459, 20K03958). K.M. is supported by JSPS KAKENHI grant No. JP19J12892. M.K. is supported by NSFC Research Fund for International Young Scientists (11850410441). Y.L. is supported by JSPS KAKENHI grant No. 19J22167. M.A.F. and A. B.B. acknowledge support from the NAOJ Visiting Professor program.

### ORCID iDs

Michael Famiano https://orcid.org/0000-0003-2305-9091
A. Baha Balantekin https://orcid.org/0000-0002-2999-0111
T. Kajino https://orcid.org/0000-0002-8619-359X
M. Kusakabe https://orcid.org/0000-0003-3083-6565
K. Mori https://orcid.org/0000-0003-2595-1657
Y. Luo https://orcid.org/0000-0002-8965-1859

```
References
Adelberger, E. G., Austin, S. M., Bahcall, J. N., et al. 1998, RvMP, 70, 1265
Alastuey, A., & Jancovici, B. 1978, ApJ, 226, 1034
Arcones, A., Martínez-Pinedo, G., Roberts, L. F., & Woosley, S. E. 2010,
      A, 522, A25
Arlandini, C., Käppeler, F., Wisshak, K., et al. 1999, ApJ, 525, 886
Beun, J., McLaughlin, G. C., Surman, R., & Hix, W. R. 2008, PhRvC, 77,
Boyd, R. N. 2008, An Introduction to Nuclear Astrophysics (Chicage, IL:
  Univ. Chicago Press), 154
Clayton, D. D. 1983, Principles of Stellar Evolution and Nucleosynthesis
  (Chicage, IL: Univ. Chicago Press), 359
Dewitt, H. E., Graboske, H. C., & Cooper, M. S. 1973, ApJ, 181, 439
Famiano, M. A., Balantekin, A. B., & Kajino, T. 2016, PhRvC, 93, 045804
Fassio-Canuto, L. 1969, PhRv, 187, 2141
Graboske, H. C., Dewitt, H. E., Grossman, A. S., & Cooper, M. S. 1973, ApJ,
Grasso, D., & Rubinstein, H. R. 2001, PhR, 348, 163
Hardy, J. C., & Towner, I. S. 2009, PhRvC, 79, 055502
Harikae, S., Takiwaki, T., & Kotake, K. 2009, ApJ, 704, 354
Ichimaru, S. 1993, RvMP, 65, 255
Illiadis, C. 2007, Nuclear Physics of Stars (New York: Wiley-VCH), 147
Itoh, N., Hayashi, H., Nishikawa, A., & Kohyama, Y. 1996, ApJS, 102, 411
Itoh, N., Tomizawa, N., Tamamura, M., Wanajo, S., & Nozawa, S. 2002, ApJ,
Itoh, N., Totsuji, H., & Ichimaru, S. 1977, ApJ, 218, 477
Itoh, N., Totsuji, H., Ichimaru, S., & Dewitt, H. E. 1979, ApJ, 234, 1079
Jancovici, B. 1977, JSP, 17, 357
```

Kapusta, J. I., & Gale, C. 2006, Finite-Temperature Field Theory: Principles

Kiuchi, K., Cerdá-Durán, P., Kyutoku, K., Sekiguchi, Y., & Shibata, M. 2015,

and Applications (Cambridge: Cambridge Univ. Press)

Kawasaki, M., & Kusakabe, M. 2012, PhRvD, 86, 063003

PhRvD, 92, 124034

```
Kiuchi, K., Kyutoku, K., Sekiguchi, Y., Shibata, M., & Wada, T. 2014,
  PhRvD, 90, 041502
Kodama, T., & Takahashi, K. 1975, NuPhA, 239, 489
Kozyreva, A., Gilmer, M., Hirschi, R., et al. 2017, MNRAS, 464, 2854
Kravchuk, P. A., & Yakovlev, D. G. 2014, PhRvC, 89, 015802
Liu, J.-J. 2016, RAA, 16, 83
Liu, M. Q., Zhang, J., & Luo, Z. Q. 2007, A&A, 463, 261
Luo, Y., Famiano, M. A., Kajino, T., Kusakabe, M., & Balantekin, A. B. 2020,
   PhRvD, 101, 083010
Meyer, B. S., & Adams, D. C. 2007, M&PSA, 42, 5215
Mumpower, M. R., Kawano, T., Sprouse, T. M., et al. 2018, ApJ, 869, 14
Nakamura, K., Kajino, T., Mathews, G. J., Sato, S., & Harikae, S. 2015, A&A,
   582, A34
Nakamura, K., Takiwaki, T., Kotake, K., & Nishimura, N. 2012, in IAU Symp.
   279, Death of Massive Stars: Supernovae and Gamma-Ray Bursts, ed.
   P. Roming, N. Kawai, & E. Pian (Cambridge: Cambridge Univ. Press), 365
Paxton, B., Bildsten, L., Dotter, A., et al. 2011, ApJS, 192, 3
Paxton, B., Marchant, P., Schwab, J., et al. 2015, ApJS, 220, 15
Paxton, B., Schwab, J., Bauer, E. B., et al. 2018, ApJS, 234, 34
Potekhin, A. Y., & Chabrier, G. 2013, Copp, 53, 397
Price, D. J., & Rosswog, S. 2006, Sci, 312, 719
```

```
Quarati, P., & Scarfone, A. M. 2007, ApJ, 666, 1303
Ruiz, M., Tsokaros, A., & Shapiro, S. L. 2020, PhRvD, 101, 064042
Sahoo, B. K., & Das, M. 2016, EPJD, 70, 270
Salpeter, E. E. 1954, AuJPh, 7, 373
Salpeter, E. E., & van Horn, H. M. 1969, ApJ, 155, 183
Shalybkov, D. A., & Yakovlev, D. G. 1987, Ap, 27, 562
Shaviv, G., & Shaviv, N. J. 2000, ApJ, 529, 1054
Shibagaki, S., Kajino, T., Mathews, G. J., et al. 2016, ApJ, 816, 79
Spera, M., & Mapelli, M. 2017, MNRAS, 470, 4739
Spitaleri, C., Bertulani, C., Fortunato, L., & Vitturi, A. 2016, PhLB, 755, 275
Suda, T., Katsuta, Y., Yamada, S., et al. 2008, PASJ, 60, 1159
Suzuki, T., Shibagaki, S., Yoshida, T., Kajino, T., & Otsuka, T. 2018, ApJ,
  859, 133
Takahashi, K., Yoshida, T., & Umeda, H. 2018, ApJ, 857, 111
Takiwaki, T., Kotake, K., & Sato, K. 2009, ApJ, 691, 1360
Vassh, N., Vogt, R., Surman, R., et al. 2019, JPhG, 46, 065202
Wallace, R. K., Woosley, S. E., & Weaver, T. A. 1982, ApJ, 258, 696
Wang, B., Bertulani, C. A., & Balantekin, A. B. 2011, PhRvC, 83, 018801
Wang, M., Audi, G., Kondev, F. G., et al. 2017, ChPhC, 41, 030003
Woosley, S. E. 2017, ApJ, 836, 244
Wu, Y., & Pálffy, A. 2017, ApJ, 838, 55
```